A Multiphysics approach to constrain the dynamics of the Altiplano-Puna magmatic system

A. Spang[1], T. S. Baumann[1], B. J. P. Kaus[1,2]

[1]Johannes Gutenberg University, Institute of Geosciences, Johann-Joachim-Becher-Weg 21, 55128 Mainz, Germany

[2]TeMaS, Terrestrial Magmatic Systems Research Center, temas.uni-mainz.de

Corresponding author: Arne Spang (arspang@uni-mainz.de)

This manuscript has been peer reviewed and was accepted for publication by JGR Solid Earth.
DOI: 10.1029/2021JB021725

A Multiphysics approach to constrain the dynamics of the Altiplano-Puna magmatic system

A. Spang [1], T. S. Baumann [1], B. J. P. Kaus [1,2]

[1]Johannes Gutenberg University, Institute of Geosciences, Johann-Joachim-Becher-Weg 21, 55128 Mainz, Germany
[2]TeMaS, Terrestrial Magmatic Systems Research Center, temas.uni-mainz.de

Key Points:

- 3D visco-elasto-plastic thermomechanical modelling of the Altiplano-Puna magma system, constraining density, melt content and geometry of the APMB
- Joint, dynamically consistent, interpretation of seismic imaging, gravity anomalies and surface velocities, including uncertainty estimation
- APMB has a central rise of about 80 km diameter, a density contrast of 90 - 130 kg/m^3 to the crust and a melt content of 15 - 22 %

Corresponding author: Arne Spang, arspang@uni-mainz.de

This article has been accepted for publication and undergone full peer review but has not been through the copyediting, typesetting, pagination and proofreading process, which may lead to differences between this version and the Version of Record. Please cite this article as doi: 10.1029/2021JB021725.

Abstract
Continuous Interferometric Synthetic Aperture Radar (InSAR) monitoring (> 25 years) has revealed a concentric surface deformation pattern above the Altiplano-Puna magma body (APMB) in the central Andes. Here, we use a joint interpretation of seismic imaging, gravity anomalies and InSAR data to constrain location, 3D geometry and density of the magma body. By combining gravity modelling, thermomechanical modelling, scaling law analysis and Bayesian inference, we are able to create a relationship between the geometry of a mid-crustal magma body and surface observations. Furthermore, we can estimate the uncertainties associated with the geometry of the APMB and identify the most important parameters that control the dynamics of the system. We constrain the density contrast between the APMB and the surrounding host rock to 90 - 130 kg m^{-3} (2σ) and the associated melt fraction to 15 - 22 %. Our visco-elasto-plastic 3D thermomechanical model reproduces the observed surface deformation self-consistently by buoyancy driven magma transport without the need for additional pressure sources. The flow pattern is controlled by a central rise at the top of the APMB whose geometry can be constrained with the help of InSAR observations while Bouguer anomalies constrain the deeper parts of the APMB. Automated scaling law analysis shows that the rheology of the upper crust and the magma mush as well as the density contrast between the two are the most important parameters in the system and need to be constrained for a better understanding of the subsurface processes.

Plain Language Summary

Volcanoes can have a big impact on economic infrastructure, the security of the population and the creation of ore deposits. They are fed and controlled by magmatic systems in the crust beneath them and we currently have no techniques to directly observe these systems. In our study, we show how numerical (computer) models that obey the laws of physics allow us to compute the observations that we would make at the surface, given a certain set of physical and geometrical parameters. By automatically changing these parameters and comparing our modelling results to real surface observations, we can discover which parameter ranges and combinations are likely. This way, we can constrain location, size, geometry, density and melt content of the Altiplano-Puna magma body in the central Andes, using only surface observations. We are able to show that different surface observables are sensitive to different parts of the magmatic system which emphasizes the importance of including multiple data sets and modelling techniques in numerical studies.

Index Terms

1211 Non-tectonic deformation
1219 Gravity anomalies and Earth structure
1295 Integration of techniques
3275 Uncertainty quantification
8439 Physics and chemistry of magma bodies

Keywords

3D geodynamic modelling, gravity modelling, variable geometry, parameter sensitivity, Bayesian inference, APMB

1 Introduction

The existence of large scale partially molten regions in the crust where mantle derived melts can accumulate, differentiate, mix and assimilate to eventually ascend towards the surface or crystallize to build plutonic bodies is a widely accepted concept in geology. With the impact that volcanic eruptions can have on economic infrastructure (e.g., Ajtai et al., 2010) and the security of the population (e.g., Naranjo et al., 1986) as well as the importance of magmatic systems in the creation of ore deposits (e.g., Hedenquist & Lowenstern, 1994), the comprehension of such systems is highly relevant. Yet, due to our inability to directly observe the dynamics within magmatic systems or to recreate lab scale models with realistic pressure and temperature conditions, our understanding remains incomplete. Numerical models that obey the laws of physics can however go beyond the limits of observations or laboratory experiments and can shed light on previously unexplored processes. Instead they are limited by the availability and quality of data as well as the complexity of a system. Here, we want to demonstrate the advantages of using joint interpretations of different data sets and physically consistent thermomechanical models.

The Altiplano-Puna volcanic complex (APVC) (De Silva, 1989) and the associated Altiplano-Puna magma body (hereafter APMB) (Chmielowski et al., 1999) in the central Andes (Figure 1) are an excellent setting for such a study as the recent research project PLUTONS (http://plutons.science.oregonstate.edu/) has provided a lot of data to base a numerical model upon (Pritchard et al., 2018; Pritchard & Gregg, 2016). Large parts of the research area are located more than 3 km above sea level (asl) and host a chain of volcanoes related to the subduction of the Nazca plate beneath south America (Godoy et al., 2014). The eruption products are dominated by dacitic to andesitic lava flows and dacitic ignimbrites (e.g., De Silva, 1989; Godoy et al., 2014; Kay et al., 2010; Wörner et al., 2018).

Pritchard and Simons (2002) reported that they observed a 70 km wide, concentric uplift pattern centered around the dormant stratovolcano Uturuncu, using Interferometric synthetic-aperture radar (InSAR) data provided by the ESA. A decade later, Fialko and Pearse (2012) as well as Henderson and Pritchard (2013) identified a 150 km wide ring of subsidence surrounding the uplifting area and showed that the pattern had been stable since 1992. With the help of levelling and GNSS data, Gottsmann et al. (2018) argued that the uplift rate has even been constant since 1965. So far, a sizable number of studies have successfully attempted to reproduce the symmetric pattern with models of varying complexity and propose inflating magma bodies in depths ranging from 5 to 40 km below sea level. Pritchard and Simons (2004); Henderson and Pritchard (2013); Walter and Motagh (2014); Henderson and Pritchard (2017); Kukarina et al. (2017) use a purely elastic, Hickey et al. (2013) a linear-visco-elastic and Hickey and Gottsmann (2014); Gottsmann et al. (2017) a temperature-dependent visco-elastic rheology. The most complex study of the area to date is a 3D model with an elastic upper crust overlying a temperature- and strain rate-dependent visco-elastic lower crust, including buoyancy effects (Fialko & Pearse, 2012). Similarly advanced models exist for other magmatic systems as well (e.g., Pearse & Fialko, 2010; Hickey et al., 2016).

One component missing from all previous studies is the consideration of plastic failure. Reuber et al. (2018b) applied a model that includes plasticity and a complex initial geometry on top of the mechanics used by Fialko and Pearse (2012) to the Yellowstone magmatic system. We will use such a state-of-the-art thermomechanical code in combination with gravity modelling and a new way to parameterize complex 3D bodies to create a relationship between the geometry of a mid-crustal magma body and surface observations. Seismic imaging, Bouguer anomalies and InSAR data will help us constrain the geometrical and physical properties of the APMB as well as its dynamics.

2 Data and Methods

We attempt to find a model geometry which is consistent with as many different observables as possible. For the location, shape, size and density of the APMB, we consider results from seismic imaging, Bouguer anomalies, InSAR as well as geochemical analysis of the eruption products of Uturuncu. To describe the background lithosphere, we consider seismic imaging and Bouguer anomalies as well as established density models of the area.

Figure 1. Topographic map of the study area, including seismic stations used in imaging studies. Green circles denote the stations used by Zandt et al. (2003) and Chmielowski et al. (1999) and the dashed green lines show the extent of the APMB, proposed by Zandt et al. (2003). Red squares denote stations used by Ward et al. (2014) and the dashed red line shows their suggestion of the maximum APMB extent. Dark blue stars denote the stations used by McFarlin et al. (2018) and Kukarina et al. (2017) while the yellow square shows the extent of the resistivity model of Comeau et al. (2016). Solid dark green line shows ANCORP reflection and magnetotellurics profile (Brasse et al., 2002; Oncken et al., 2003). White lines show extent of the "sombrero pattern" (Fialko & Pearse, 2012). Dashed magenta line shows the lateral extent of the best fitting APMB in our model at its widest part (15 km depth).

All measures of depth in this study are in reference to sea level. In sections 2.1 to 2.3, we describe the data, used in this study while sections 2.4 to 2.6 focus on creating the model setup. Section 2.7 gives details on the thermomechanical code, we use to perform numerical modelling.

2.1 Imaging Surveys

Imaging studies inferring the presence of magma in the central Andean crust date as far back as the 1980s (e.g., Schwarz et al., 1984; Breitkreuz & Zeil, 1984; Wigger, 1988). Starting with Chmielowski et al. (1999), a large number of studies have identified a layer, that they suggest to be the APMB or more generally a zone of partial melting. Chmielowski et al. (1999) and Zandt et al. (2003) interpreted the very low velocity zones ($V_s < 1.0$ km s^{-1}) in their shear wave models to be partially molten and thus conclude the APMB to be a sill like structure of less than 1 km thickness in about 15 km depth. The more recent study of Ward et al. (2014) combined receiver functions and ambient noise tomography to develop a V_s-model covering an area of about 400 x 400 km, extending to a depth of 50 km. The authors argue that any velocity lower than 2.9 km s^{-1} indicates the presence of melt and therefore suggest the APMB to extend from about 5 to 22 km depth. The concept of this shallow top of the partially molten zone is supported by the shallow brittle-ductile transition zone (BDTZ) around sea level, proposed by Jay et al. (2012). A magnetotellurics (MT) survey by Comeau et al. (2015, 2016) imaged a zone of low electrical resistivity (< 3 Ωm) starting at 14 km depth in the vicinity of Uturuncu and the authors acknowledge that their study does not allow for good estimates of the body's thickness. Most recently, McFarlin et al. (2018) presented a common conversion point stack of receiver functions, covering an area of about 100 x 100 km and imaged the top of the 9 km thick APMB at about 8 km depth. The V_p-model of Oncken et al. (2003) shows a thin layer at 12 to 15 km depth but as their profile is further north, and considering the extent suggested by Zandt et al. (2003); Ward et al. (2014), this study might be imaging the edge of the body. Supplementary Figure S1 summarizes the various suggestions for the extent of the APMB beneath its central volcano Uturuncu.

Using the same stations as McFarlin et al. (2018) and travel time inversion, Kukarina et al. (2017) present a distinctly different feature beneath Uturuncu, which is only 20 km in diameter and extends from about 5 km down to 40-80 km (depending on the isocontour) depth. The V_p-model of Heit et al. (2008) shows low velocities in the entire lithosphere which coincides with low electrical resistivities reported by Brasse et al. (2002); Kühn et al. (2018).

Considering that the overwhelming majority of studies, including the large scale

Figure 2. (a) Average LOS (line of sight) velocity from 1992 to 2010 from Fialko and Pearse (2012) around Uturuncu volcano. Circles correspond to the region of uplift (inner) and subsidence (outer) and are identical to the ones in Figures 1, 3a and 7. (b) Total vertical displacement of the center of uplift over time (Lau et al., 2018).

tomography of Yuan et al. (2000), image a low velocity zone within the upper half of the crust, we will focus on this scenario. The presence of partially molten areas in the lower crust is likely but the available geophysical constraints on their size and location are not sufficient to include them in the model.

2.2 InSAR Data

We use surface deformation data to check the results of our forward models. Fialko and Pearse (2012) present gridded average line of sight (LOS) velocities from 1992 to 2010 and Lau et al. (2018) show how the maximum velocity has evolved from 1992 to 2018 (Figure 2). Both data sets are available at https://igppweb.ucsd.edu/∼fialko/data.html. To compare our modelling results to LOS velocities, we need to project them into LOS direction according to:

$$\Delta LOS = [U_n sin(\phi) - U_e cos(\phi)] sin(\lambda) + U_z cos(\lambda) \quad (1)$$

where ΔLOS is LOS velocity, U_n , U_e and U_z are the north, east and vertical component of the velocity vector respectively, ϕ is the azimuth (flight direction) of the satellite and λ is its incidence angle (Fialko et al., 2001). We use $\phi = -167.5$ and $\lambda = 21.5$ which are the averages between the two similar descending satellite tracks (ERS 10 and 282) used to create the LOS data set (Henderson & Pritchard, 2017).

2.3 Gravity Data

To help constrain the location and properties of the APMB, we consider gravity data. We compared the Bouguer anomaly grid (EGM2008, gravity_anomaly_bg, 0.05° resolution, 6 Sigma Gaussian filter with 75 km length) from the International Center for Global Earth Models (ICGEM, http://icgem.gfz-potsdam.de/home, Barthelmes and Köhler (2016)) for the area of interest with the large regional data set of the Collaborative Research Center 267 (SFB 267), presented in Götze and Kirchner (1997) (http://www.cms.fu-berlin.de/sfb/sfb267/results/data_catalogue/central_andean_data/gravitiy_data.html). Both data sets agree well (Figure 3c) and we decided to use the grid of the ICGEM (Figure 3a) for its regular resolution and larger area coverage.

2.4 Constraining the Magma Body's Geometry

The center of our thermomechanical model is the APMB, whose shape, size and location we can constrain with the aforementioned insights from seismic imaging and gravity. We use the open source software geomIO (https://bitbucket.org/geomio/geomio, Bauville and Baumann (2019)) to create the 3D bodies that make up the system as it allows for the creation of 3D objects from drawn 2D slices and also provides an option to forward model the Bouguer anomaly of the created objects, using the approach of Talwani et al. (1959). To reproduce the gravity signal in a large mountain belt like the Andes, it is important to consider the influence of the thickened Andean crust, or more precisely, the

Figure 3. (a) Bouguer anomaly for the area of interest downloaded from the ICGEM (Barthelmes & Köhler, 2016) and low-pass filtered with a cut-off wavelength of 75 km. Black dots show gravity stations used for the regional SFB 267 survey. Dashed red line shows the extent of the APMB suggested by Ward et al. (2014). White lines show extent of the "sombrero pattern" (Fialko & Pearse, 2012). Thin black dashed lines show areas of different weights for eq. 2. The map covers the area between 69.5° W and 65° W as well as between 24.5° S and 20° S. (b) Bouguer anomaly of our version of the crustal root (same colorbar as in a). (c) Bouguer anomaly (g_B) along the EW-profiles in a and b for the data sets of the ICGEM (red solid) and the SFB 267 (red dashed). Blue dashed line shows the signal produced by our crustal root geometry and blue solid line shows the combined signal of crustal root and APMB.

Figure 4. Results of the joint interpretation of seismic imaging and gravity data. (a) Our reference model of the APMB (blue) in comparison with the 2.9 km s $^{-1}$ isocontour from Ward et al. (2014) (red). (b) Gravity signal produced by the blue body in a. (c) Misfit of the signal in b to the data shown in Figure 3a.

crustal root that provides the necessary buoyancy for the large mountain masses. Its signal is evident in Figure 3a as the entire plateau shows Bouguer anomalies of about -350 mGal.

The root is approximated as a buoyant body (lower crust surrounded by denser mantle material) extending from 35 km depth to the Moho. We consider 3 different studies for constraints on Moho depth and density of lower crust and upper mantle (Prezzi et al., 2009; Tassara & Echaurren, 2012; Laske et al., 2013). Results show that a density contrast of 390 kg m^{-3} between crustal root and upper mantle, which is in the middle of the range of the aforementioned studies, allows us to reproduce the background gravity signal well (supplementary Figure S5).

Figure 3b shows the signal produced by the constructed crustal root to be in line with the observed Bouguer anomaly. The disparity between the calculated signal of the crustal root (dashed blue line) and the observed signal (red lines) in Figure 3c is interpreted to be the contribution of the APMB which we added as a second buoyant body in the crust. As we have no constraints on the exact distribution of material within the APMB and as gravity signals tend to average out small scale signals, we assumed the APMB to have a homogeneous density contrast to the surrounding crust. Depth, size and geometry were oriented towards the 2.9 km s^{-1} isocontour from Ward et al. (2014), but the body had to be extended and slimmed in the south to get a better fit to the gravity data (Figure 4). For the APMB, we found a $\Delta\rho$ of 125 kg m^{-3} to produce a good fit, which is similar to what Potro et al. (2013) and Gottsmann et al. (2017) use. The deviation from the data in the area above the APMB is ± 20 mGal (Figure 4b) and the biggest error is in the area of the Central Andean Gravity High (CAGH) (Götze & Krause, 2002), a dense body which is not part of our model.

2.5 Gravity Inversion

Previous studies have used geophysical surface observations to constrain density and rheology simultaneously, but have assumed a constant model geometry (Baumann & Kaus, 2015). Here, we improve the approach by taking a variable geometry of the APMB

Figure 5. Setup for thermomechanical models based on crustal structure studies and our gravity analysis for crustal root and magma body. Vertical exaggeration: 2. Details on the material properties in table S1. Details on the synthetic topography in supplementary text S2.

into account, which allows us to investigate the relationship between the geometry of the magma body and the surface observations. The non-unique nature of gravity anomalies allows for a range of solutions as there is a trade-off between the density contrast of a body and its volume. To estimate the extent of realistic parameter combinations, we test a large number of different geometries and density contrasts which we generate automatically based upon our hand drawn reference model (Figure 4a). Supplementary text S1 describes our methodology for geometry variation. We use 2 control polygons (in 8.9 and 11.1 km depth) and the stretch factors Sx_1, Sx_2, Sy_1 and Sy_2 to transform the body in x(EW)- and y(NS)-direction (Figure 6f+g).

We then model the Bouguer anomaly of the geometry and compute the misfit between each model and the data, using a weighted RMS misfit function:

$$\Phi = \sqrt{\frac{\sum w_i (gB_{mod,\ i} - gB_{obs,\ i})^2}{\sum w_i}} \tag{2}$$

where Φ is the misfit of a model, gB_{mod} and gB_{obs} are the modelled and observed Bouguer anomalies respectively and w is the weight of the grid point. Every grid point inside a radius of 100 km from the location of the lowest Bouguer anomaly received the weight 1, while every grid point inside an ellipse with semi-major axes 120 (EW) and 200 (NS) km received a weight of 0.5 (Figure 3a). This allows us to exclude the effect of the (CAGH) (Götze & Krause, 2002), which is not part of our model, and limit the influence of grid points outside of the APMB's signal. We generate an initial set of 32768 (8^5) unique models using uniformly distributed values in the range of 0 and 250 $\mathrm{kg\,m^{-3}}$ for $\Delta\rho$ and in the range of 0.1 and 2.0 for the stretch factors. Next, we use the neighborhood algorithm (Sambridge, 1999a) to produce another 60000 models in areas of low misfit.

2.6 Lithospheric Structure

For the lithospheric structure surrounding the APMB, we use a horizontally layered compromise between the global model crust 1.0 (Laske et al., 2013) and three regional crustal models based on rock chemistry and gravity inversion (Prezzi et al., 2009; Tassara & Echaurren, 2012; Ibarra et al., 2019) summarized in supplementary Figure S5. Sparks et al. (2008) studied the eruption products of Uturuncu and reported dacitic lavas with up to a few wt% of andesitic inclusions, concluding the APMB to be build by a lower layer of intruding andesites and an upper layer of more evolved dacites which are the product of differentiation and extensive crustal melting. This concept is supported by isotope studies (e.g., Kay et al., 2010; Michelfelder et al., 2014; Godoy et al., 2017; Wörner et al., 2018), which is why we split the APMB into a more viscous, dacitic, upper and a less viscous, andesitic, lower part. We put the boundary between both parts at the same depth as the upper crust/middle crust interface as we expect the andesites to naturally stall at this buoyancy boundary. Table S1 summarizes the material parameters and Figure 5 shows the setup used for the thermomechanical models.

2.7 Thermomechanical Model

For our models we use the 3D thermomechanical finite differences code LaMEM (Kaus et al., 2016). It solves for the conservation of momentum, mass and energy (eq. 3-5), using a staggered grid in combination with a marker-in-cell approach (Harlow &

Welch, 1965). Along the boundaries of the setup, we apply free slip conditions, allowing velocities > 0 parallel to the walls while setting perpendicular velocities to 0. At the top of the setup, we include about 10 km of sticky air above the stabilized free surface (Kaus et al., 2010; Duretz et al., 2011; Crameri et al., 2012).

$$\frac{\partial \tau_{ij}}{\partial x_j} - \frac{\partial p}{\partial x_i} + \rho g_i = 0 \tag{3}$$

$$\frac{1}{K}\frac{Dp}{Dt} - \alpha \frac{DT}{Dt} + \frac{\partial v_i}{\partial x_i} = 0 \tag{4}$$

$$\rho C_p \frac{DT}{Dt} = \frac{\partial}{\partial x_i}\left(\lambda \frac{\partial T}{\partial x_i}\right) + H \tag{5}$$

τ_{ij} is the Cauchy stress deviator, $x_i (i = 1,2,3)$ denotes the Cartesian coordinates, p is pressure (positive in compression), ρ density, g_i gravitational acceleration, K the bulk modulus, α the thermal expansion coefficient, T the temperature, v_i the velocity vector, C_p the specific heat capacity, λ the thermal conductivity, H the volumetric heat source and D/Dt is the material time derivative. The rocks are characterized by a visco-elasto-plastic rheology where the strain rate is the sum of the elastic, viscous and plastic components:

$$\dot{\epsilon}_{ij} = \dot{\epsilon}^{el}_{ij} + \dot{\epsilon}^{vi}_{ij} + \dot{\epsilon}^{pl}_{ij} \tag{6}$$

$\dot{\epsilon}_{ij}$ denotes the total deviatoric strain rate tensor, while $\dot{\epsilon}^{el}_{ij}$, $\dot{\epsilon}^{vi}_{ij}$ and $\dot{\epsilon}^{pl}_{ij}$ represent the elastic, viscous and plastic strain rate components. For a detailed discussion of this equation and all of its components, the reader is referred to Kaus et al. (2016). Here we will focus on the material parameters which impact the 3 components.

The elastic component is controlled by the shear modulus G, which we compute from an averaged profile from Ward et al. (2017) (table S1). We also consider the rocks to be compressible and use a Poisson's ratio ν of 0.2 for all crustal rocks and the mantle (Gercek, 2007).

The viscous component is characterized by the viscosity η, which follows the temperature- and strain rate-dependent powerlaw relationship of dislocation creep:

$$\eta = \frac{1}{2}(B_n)^{-\frac{1}{n}} (\dot{\epsilon}_{II})^{\frac{1}{n}-1} \exp\left(\frac{E_n}{nRT}\right), \tag{7}$$

where B_n is the creep constant, $\dot{\epsilon}_{II}$ the square root of the second invariant of the strain rate ($\dot{\epsilon}_{II} = (\frac{1}{2}\dot{\epsilon}_{ij}\dot{\epsilon}_{ij})^{1/2}$), E_n the activation energy, n the powerlaw exponent, R the universal gas constant and T the temperature. All viscous parameters are summarized in table S1.

The plastic component is controlled by the yield strength τ_{yield}, which depends on the pressure p as well as the material parameters cohesion c_0 and friction angle ϕ:

$$\tau_{yield} = \sin(\phi) p + \cos(\phi) c_0 \tag{8}$$

Equation 8 corresponds to the Drucker-Prager failure criterion (Drucker & Prager, 1952) which is a good approximation of Byerlee's law (Byerlee, 1978). Most research on magmatic rock friction angles is limited to granites and results usually vary around 30° (Jang et al., 2018). Cohesion estimates for intact rocks typically range around a few MPa (e.g., Hoek & Brown, 1997). Therefore we use $\phi = 30°$ and $c_0 = 10$ MPa for all rocks.

We use 256 cells in each horizontal direction and 128 cells in the vertical. This yields roughly 8.5 million cells and a horizontal resolution of 1.95, as well as a vertical resolution of 0.74 km. As we are interested in the present day state of the system, we only run the model for two time steps. The first timestep is not considered, as there is still influence of isostatic balancing between topography and Moho. From the second timestep onward, the surface velocities are dominated by the buoyancy of the magma body.

Figure 6. (a-c) Misfit (Φ) in dependence of sets of 2 parameters. Note that each dot in the areas of high misfit is the best fitting model of 512 (8^3) versions that all plot on the same coordinate when they are projected in this 2-dimensional parameter space due to the regular gridded initial models. (d-e) Posterior probability density functions (PDF) resulting from resampling the gravity models. (d) PDF for density contrast $\Delta\rho$, showing it to be 111 $\pm$ 9.7 kg m^{-3}. (e) PDF for Sx_1 in solid red, Sy_1 in dashed red, Sx_2 in solid blue and Sy_2 in dashed blue. This shows that the geometry of the lower part of the APMB (Sx_1 and Sy_1) is well constrained and can be described by Gaussian distributions. The opposite is the case for the upper part (Sx_2 and Sy_2). (f) Sketch to show how Sx and Sy affect a single polygon (dashed = original, solid = new). (g) 3D view of reference APMB. Everything below control polygon 1 (red) is affected by Sx_1 and Sy_1, while everything above control polygon 2 (blue) is affected by Sx_2 and Sy_2. Central part is affected by both sets.

3 Results

3.1 Gravity Inversion

To visualize the results of the gravity inversion, we plot the misfit of each individual model in dependence of 2 out of the 5 parameters. Figure 6a-c show a selection of the most important ones while a full overview can be found in Figure S2. There is a good correlation between $\Delta\rho$, Sx_1 and Sy_1 with the best fitting models being constrained between 80 to 130 kg m^{-3} and 0.8 to 1.3, respectively (Figure 6a,b). Sx_2 and Sy_2 show large spread with the range of low misfit models being controlled by $\Delta\rho$, Sx_1 and Sy_1 entirely (Figure 6c). This demonstrates that the lateral extent of the APMB is poorly constrained for the upper part of the magma body. We also performed an independent set of 1000 models, only varying $\Delta\rho$ and the vertical extent of the APMB (S_z). The results are displayed in supplementary Figure S3a and show that a $\Delta\rho$ of roughly 200 kg m^{-3} would be necessary to fit the Bouguer anomaly with a magma body of 9 km thickness as proposed by McFarlin et al. (2018). We therefore decided to keep the thickness of the APMB fixed to the extent suggested by Ward et al. (2014) to reduce the parameter space to a reasonable size for our investigation.

To obtain a more quantitative result, we follow a Bayesian inversion strategy and resample the parameter space with the rejection approach described by Sambridge (1999b). We use uniformly distributed random numbers in the ranges of 0 to 250 kg m^{-3} for $\Delta\rho$ and 0.1 to 2.0 for all stretch parameters as our priors. The resampling algorithm is described in more detail in supplementary text S4 and Figures 6d+e summarize the results. The accepted samples for $\Delta\rho$ show a normal distribution with a mean (μ) of 111 kg m^{-3} and a standard deviation (σ) of 9.7 kg m^{-3}. The stretch factors for the lower control polygon Sx_1 and Sy_1 are also normally distributed with μ = 1.04 and 1.23 respectively and σ = 0.08 and 0.12. Samples for Sx_2 and Sy_2 which are related to the upper control polygon show no bell curve distribution but are instead found within the entire range with Sy_2 trending towards the lower and Sx_2 towards the upper end.

Figure 7. Comparison between InSAR data and the surface velocities of different models projected into LOS. Solid and dashed circles are for orientation and are identical to the ones in Figures 1, 2 and 3. (a) InSAR data. (b) Result of the geometry, solely constrained by seismic imaging and gravity. (c) Results after altering location and geometry of central rise and basis for the 2nd row. (d) Variation of c with a lower density mush. (e) Variation of c with a higher powerlaw exponent in the flow law of the upper crust. (f) Variation of c with a higher shear modulus in the mantle. Sketches above b and c are vertically exaggerated 2D-EW slices of the APMB that illustrate, how the shape of the central rise was changed between them.

Figure 8. Velocity field inside and around APMB for the reference case (a) and a case where the central rise was narrowed to 50% of its diameter (b). Shaded areas show vertical velocity in the crust above the magma body. Areas between -0.1 and 0.3 cm/yr were made completely transparent for better visibility of the relevant features. Insets show the corresponding surface deformation, using the colorbar of Figure 7.

3.2 Thermomechanical Models

Using the magma body, constrained by seismic imaging and gravity modelling, we performed forward models in LaMEM to predict surface velocities and used eq. 1 to project them into line of sight direction. While the result did show areas of uplift and areas of subsidence, the pattern did not match the InSAR observations (Figure 7b). It was however apparent that the uplifting area was overlying the central rise of the APMB (i.e. where it was shallowest). As the spatial resolution of seismic imaging and gravity do not allow to constrain smaller scale features of the APMB, we altered the location and geometry of the central rise and achieved an improved fit to the InSAR data (Figure 7c). The model produces a circular, 80 km wide area of positive ΔLOS, with peak velocities of 1.1 - 1.2 cm/yr. Around the uplifting area, there is a diffuse ring of subsidence with ΔLOS of -0.3 to 0 cm/yr and a diameter of roughly 150 km. The ring is broken in the northwest and east where we find areas of minor (ΔLOS < 0.3 cm/yr) uplift and the remaining surface does not move noticeably. We also reproduce the 6 km westwards shift of peak ΔLOS when projecting the surface velocities into the ascending satellite track ENVISAT 89 ($\phi = -13$ and $\lambda = 41.1$), as reported by (Fialko & Pearse, 2012).

Taking a look at the velocity field inside and around the APMB shows that material is flowing from the outskirts of the APMB towards the central rise and upwards, pushing the overlying crust up and creating the concentric area of uplift (Figure 8a). At the same time, the crust overlying the parts of the APMB that are drained from sinks down, creating the ring of subsidence at the surface. There is also some minor flow towards the NW- and NE-edge of the magma body, corresponding to the two areas of minor uplift (Figure 7c). Given the aforementioned uncertainty in the geometry of the APMB's central rise, we investigated how changing it impacted the system. Figure 8b illustrates how thinning the central rise to half its diameter restricts the flow inside the APMB and weakens the surface deformation pattern.

To gain more insight into the parameters that the model is sensitive to, we performed an automated sensitivity testing for the vertical velocity at the summit of Uturuncu following the approach of Reuber et al. (2018a). With a model and parameter set that can match the observations well, we can compute the finite-difference gradients of all parameters as well as a scaling law that describes how influential individual parameters are

Figure 9. Automatically computed scaling law exponents for all parameters. The absolute value (|b|) of the exponent of a parameter is a measure of how strongly a relative change in that parameter would change the observation (in this case, the vertical velocity at the summit of Uturuncu). Note that not all materials use the same parameters (for instance, Dacite is characterized by linear viscosity η while the upper crust's rheology is defined by Bn, En and n). $\Delta\rho$ describes the density contrast between the magma and its associated host rock. Parameters Sx_1, Sy_1, Sx_2 and Sx_2 are geometric parameters of the APMB and T_{bot} the temperature at the bottom of the model. They are therefore not associated with any one material.

on the observation point. It has the form:

$$u_{obs} = A p_1^{b_1} p_2^{b_2} \dots p_n^{b_n} \tag{9}$$

where u_{obs} is the observed velocity, A is a pre-factor, p_1 to p_n are the model parameters and b_1 to b_n are the respective scaling law exponents. If $b_i > 0$, an increase in parameter p_i will lead to an increase in u_{obs} and vice versa for $b_i < 0$. The absolute value of the scaling law exponent describes how strongly a relative change in the respective parameter would change the observable. Figure 9 shows $|b|$ for all model parameters, with upwards pointing triangles corresponding to $b>0$ and downward pointing triangles corresponding to $b<0$.

The scaling law suggests that the rheology of the upper crust (controlled by the activation energy En, the powerlaw exponent n and indirectly by the initial temperature T of the dacitic mush) is most influential on the maximum surface deformation. It is followed by the density contrast between dacitic mush and upper crust, the elastic components (shear modulus G and poisson ratio ν) of the dacitic mush as well as the geometry of the central rise (Sx_2 and Sy_2). The plastic parameters cohesion c_0 and friction angle ϕ as well as most thermal parameters (thermal expansivity α, heat capacity Cp and thermal conductivity k) that are not associated with the upper crust or dacitic mush have little effect on the surface velocity. The lower row of Figure 7 shows that the conclusions from the scaling law exponent analysis are consistent with our forward simulation results as Figure 7e represents an increase of the powerlaw exponent of the upper crust by 20% which is associated with a strong increase in LOS velocities. In Figure 7f, the shear modulus of the mantle was increased by 20% with little to no effect on the surface displacement. Figure 7d shows how changing the density contrast between crust and mush by 20% affects the system.

Running the model for a longer amount of time does not affect the surface deformation pattern. Only the amplitude of the velocities decreases over time, which is to be expected as without new supply of magma, the system will eventually reach isostatic equilibrium between the buoyant mush and the surface elevation it has uplifted. Fialko and Pearse (2012) report the same observation in their diapir model.

4 Discussion

4.1 Seismic Imaging and Gravity

The joint interpretation of seismic imaging studies and gravity data provides a robust picture of the large scale geometry of the APMB which neither data set could have provided on its own. Computing more than 90'000 different interpretations also allows us to estimate its uncertainties. The analysis also supports the concept of a magma body of

Figure 10. Estimation of andesitic melt content of the lower half of the APMB in dependence of crustal density, density contrast and H_2O content. Red ellipsoid indicates the data range, assumed in this study (gray ellipses are 2D projections). Planes show melt content. Details on the calculations are found in supplementary text S3.

about 15 km in thickness, as proposed by Ward et al. (2014). Figure S3a shows that a quite high $\Delta\rho$ of $\sim$ 200 kg m^{-3} and, associated with that, a melt content in the range of 40% (Figure 10) would be necessary to fit the thickness range ($\approx$ 8 km) proposed by McFarlin et al. (2018). The case is even worse for a 1 km thin melt zone as suggested by the studies of the late 90s and early 2000s (e.g., Chmielowski et al., 1999; Zandt et al., 2003). We did not extend our calculations to that range, but the trend in Figure S3a suggests that even pure melt would not be enough to reproduce the observed Bouguer anomalies with such a thin layer. As the center of the body is roughly at the same depth in all three scenarios, it is likely that it contains the highest melt fraction.

The resampling of the gravity data (Figure 6e) shows that the extent of the APMB below 11 km depth (defined by Sx_1 and Sy_1) is well constrained by the Bouguer anomalies. In EW-direction the size of our reference model fits the Bouguer anomalies well ($\mu_{Sx_1} = 1.04$) while it should be extended in NS-direction ($\mu_{Sx_1} = 1.23$). Figure 1 shows the maximum lateral extent of our best fitting geometry. Its northern edge coincides with the ANCORP profile (Oncken et al., 2003), suggesting that the thin low velocity layer they imaged, represents the edge of the APMB. The upper part of the magma body cannot be constrained with the help of gravity data. Despite being closer to the surface, the lower mass within the central rise has too little influence on the overall signal of the APMB. It is not clear why Sx_2 trends towards high and Sy_2 towards low values but the fact that we find samples within the entire parameter range shows the small influence of these parameters for the Bouguer signal.

4.2 Melt Content

The constraints we gained on $\Delta\rho$ allow us to make estimations on the melt fraction within the APMB by assuming the APMB to be a mix of melt and crustal material, and computing the mass balance between both components. Melt density depends on its composition (table S2), including volatile components as well as temperature and pressure. Laumonier et al. (2017) proposes H_2O contents of up to 10 % for the lower andesitic part of the magma body. Figure 10 shows the correlation between density contrast, density of the crust, H_2O content and melt fraction. The red ellipsoid displays likely ranges for the density contrast (this study), density of the middle crust (Tassara et al., 2006; Prezzi et al., 2009; Laske et al., 2013; Ibarra et al., 2019) and H_2O content (Laumonier et al., 2017). Based on these ranges, the melt content in the andesitic part of the APMB should be on the order of 15-22 vol-%, which is in line with the estimation of 14-27 % based on several electrical conductivity studies (Schwarz & Krüger, 1997; Schilling et al., 2006; Comeau et al., 2015, 2016). It also coincides with the upper range of the estimation of Ward et al. (2014) (4-25%) based on the reduction of shear wave velocity and with the preferred model of Potro et al. (2013) ($\sim$25%) which is based on gravity data but proposes a different distribution of melt than this study. For the dacitic part we lack estimates for water content but assuming a similar range, we would expect about 5% more melt in the upper part of the APMB.

Figure 11. Combined results from the resampling of gravity and thermomechanical forward models. The lower sub-Figures show probability density for the stretch factors in 11.1 (Sx_1 and Sy_1) and 8.9 km depth (Sx_2 and Sy_2). White areas did not record a single sample among the accepted 20000. The upper sub-Figures show the results of the resampling of the thermomechanical models where only Sx_2 and Sy_2 were varied in black along the PDF of Sx_2 and Sy_2 from the gravity resampling in green. Right side shows another sketch of the way Sx and Sy influence a single polygon.

4.3 Thermomechanical modelling

4.3.1 The Central Rise

Modelling the thermomechanical dynamics of the system highlights that transport of mush material from the outskirts to the center of the APMB is crucial to reproduce the surface deformation pattern observed by InSAR (Figures 7 and 8). It also shows the necessity for a pronounced rise in the body. As the center of surface uplift depends on the location of the central rise and the pattern and magnitude of deformation on its shape and size, we can constrain how the APMB's shallow areas look like, which would not have been possible by only considering seismic imaging and gravity data (Figure 6e). To constrain the geometry of the central rise we ran 1000 forward models (400 initial + 600 in areas of low misfit) using 1.04 and 1.23 for Sx_1 and Sy_1 respectively, and 110 $\mathrm{kg\,m^{-3}}$ for $\Delta\rho$ while varying Sx_2 and Sy_2 in the entire range between 0.1 and 2.0. We kept the other three parameters constant as they are already well constrained from gravity and to reduce the size of the parameter space for the computationally more expensive thermomechanical models. Similarly to the gravity data, we resampled the models to get a probability distribution for Sx_2 and Sy_2, using the misfit between the modelled surface velocities projected into LOS (eq. 1) and the InSAR data (Figure 2a).

The resampling resulted in near-gaussian distributions for both stretch factors which are characterized by $\mu_{Sx2} = 0.70$ and $\mu_{Sy2} = 1.04$ as well as $\sigma_{Sx2} = 0.03$ and $\sigma_{Sy2} = 0.05$. Figure 11 combines these results with an interpolated representation of the gravity resampling. This demonstrates that analyzing the Bouguer anomalies (green curves) provides little to no constraints on the upper parts of the APMB but incorporating the thermomechanical simulations can compensate for that as the surface velocities are very sensitive to the geometry of the central rise. At the same time, the extent of the lower half of the APMB only has a negligible effect on the surface velocities. Combining the two approaches yields useful constraints on both the upper and the lower part of the magmatic system.

While the model can show the necessity for the central rise, it can not develop the rise from a flat topped APMB on its own. Consequently, it must have been initiated through some initial perturbation. One reasonable explanation is the reactivation of old pathways, as multiple geochemical studies suggest the transport of melt to small, shallow magma reservoirs around sea level prior to eruptions (Sparks et al., 2008; Muir et al., 2014a, 2014b). Another possible explanation is the fact that the crust is hottest (and therefore weakest) above the center of the APMB, facilitating magma ascent there. Lastly, this may be the area where new batches of melt are emplaced from below. Provided that the deeply rooted, tooth-shaped anomaly imaged by Kukarina et al. (2017) represents melt pathways, the last scenario would be the most likely. The depth, location and width of the central rise's top agrees well with the top of this feature (Figure 12). Ward et al. (2014) also state that they see the magma body shallowest beneath Uturuncu.

4.3.2 Key Parameters

The amplitude of the surface deformation pattern is controlled by the magnitude of material transport within the APMB, which in turn is a function of multiple quantities. The geometry of the central rise as well as the rheology of the upper crust and mush trade off against each other, so it is impossible to find a unique solution. We can, however, conclude that a change in any of them can explain the decrease in surface velocities over the past decade, as reported by Lau et al. (2018) (Figure 2b).

As both, rheology of the upper crust and of the magma mush depend on temperature, a loss of heat, possibly through waning magma supply or developing exit paths for hot fluids, would be a good candidate. Another possible scenario includes loss of volatiles or an increase in crystal content in the magma which can shift its viscosity by several orders of magnitude. This could also have a relevant effect on the surface velocities despite η_{Dacite} not ranking high in Figure 9. The possibility for a sudden (on timescales of years to decades) slowdown of surface velocities could even help to solve the paradox that Gottsmann et al. (2018) are able to show that Uturuncu has been uplifting since 1965, while Perkins et al. (2016) show geomorphic evidence for no long-term (century scale) uplift. Another reason for the absence of long-term uplift is the aforementioned isostatic equilibrium that the buoyant magma reaches with the elevation it generated by uplift.

A look at deviatoric stresses in the crust show that they are highest above the central rise between surface and sea level, which is the only area where we observe plastic yielding in our simulations (for rock cohesion of both 1 and 10 MPa). This coincides with the domain where Jay et al. (2012) and Kukarina et al. (2017) detected the bulk of local earthquakes (Figure 12).

4.4 Comparison to other Models

In this study, we present the first 3D model of the Altiplano-Puna magma system with a temperature- and strain rate-dependent visco-elasto-plastic rheology, including all deformation mechanisms that are observed for real rocks. As in the temperature-dependent visco-elastic model of Fialko and Pearse (2012), stresses are caused by density instabilities (i.e. light mush rising in a denser crust). Pritchard and Simons (2004), Hickey et al. (2013) as well as Henderson and Pritchard (2017) neglect buoyancy forces and create stresses through inflating point sources (Mogi Model (Kiyoo, 1958)) in a purely elastic or linear-visco-elastic (Hickey et al., 2013) crust. Gottsmann et al. (2017) is the only previous study that considered the entire magma body, using it as a source for depressurization, while pressurizing a vertically extending column. Figure 12 shows the different geometries proposed by the aforementioned studies.

There are some important similarities between our study and the work of Gottsmann et al. (2017), most notably the consideration of the entire APMB as an active part of the system and the presence of a central feature that attracts material. There is, however, a notable difference in the geometry of the central feature and to a lesser degree in the main body. But more importantly, Gottsmann et al. (2017) prescribe a pressure source in the vertical column (Figure 12) and a pressure sink in the rest of the body to simulate the effects of mush moving from there to the column. In our model, buoyancy forces are developing this flow of material self consistently, without a prescribed pressure source as the driving force.

An element that our study shares with the work of Fialko and Pearse (2012) is the role of buoyancy as the driving force of the system. But instead of a 10 km wide diapir of almost pure melt($\Delta\rho = 400\,\mathrm{kg\ m^{-3}}$), we consider the entire APMB as imaged by seismics and constrained by gravity as a buoyant body with a density contrast of about 110 $\mathrm{kg\ m^{-3}}$ to the surrounding crust.

Figure 12. EW slice through the shear wave velocity model from Ward et al. (2014) beneath Uturuncu. On top, the various models that reproduce the observed InSAR pattern. Solid line models are density driven, dashed lines are inflating pressure sources. Black stars show earthquake locations from Kukarina et al. (2017) and dotted purple line shows bulk of earthquake locations reported by Jay et al. (2012). Dotted red line shows the transition between magma and hybrid material from Gottsmann et al. (2017). As most of the models of Pritchard and Simons (2004) plot on top of each other, they are summarized in one circle. Henderson and Pritchard (2017) also postulate a deflating pressure source at 65 km depth, which plots outside of the Figure. Dashed black line shows the Vp/Vs = 1.9 isocontour from Kukarina et al. (2017). Bottom right: Zoomed out to cover full body. Note the vertical exaggeration.

5 Conclusions

We present a 3D nonlinear visco-elasto-plastic numerical model of the Altiplano-Puna magma system, which is consistent with observations made by seismic imaging, gravity surveys, crustal density models, earthquake locations and InSAR data. We use a joint interpretation of shear wave velocities and Bouguer anomalies to optimize the constraints on the extent of the APMB and to estimate its density contrast to the surrounding crust to be 90 - 130 kg m^{-3} (2σ). Based on that, and using crustal density models as well as the chemistry of eruption products, we can estimate the melt fraction in the lower part of the APMB to be 15-22 vol-%.

Forward models with the thermomechanical stokes code LaMEM show that the observed surface deformation can be caused by the buoyancy-driven transport of mush material from the outskirts of the APMB towards a central rise, pushing the overlying crust upwards. At the same time, the crust, overlying the areas being drained from, is subsiding in a ring-like pattern. In our model, there is no need for large intrusions (i.e. pressure sources) to reproduce the observed surface deformation. We also show the link between the geometry of the central rise and the surface deformation pattern and demonstrate that the amplitude of deformation depends mainly on the width of the rise as well as on the rheology of the upper crust and mush. Consequently, a better understanding of the rheological properties of upper crust and especially mush is necessary to improve our understanding of the dynamics of magmatic systems. Loss of heat or volatiles as well as growth of crystals are likely candidates to be currently slowing the surface deformation down and preventing long-term uplift.

Our results clearly show the advantages of using joint interpretations and physically consistent thermomechanical models, as most observables are only sensitive to parts of the system while leaving other parts unconstrained. Combining different data sets and different modelling techniques allows us to constrain more parameters and also quantify the uncertainties that the data include. Lastly, we demonstrate and quantify the influence of initial model geometries on the forward solution and recommend treating geometry as a parameter like rheology or density.

Acknowledgments
This study was funded by the European Research Council through the MAGMA project, ERC Consolidator Grant # 771143. The maps in Figures 1, 3 and 4 were created using the Generic Mapping Tool, version 5.4.3 (Wessel et al., 2013). We used perceptually uniform colormaps to prevent optical data distortion (Crameri, 2018). Parts of this research were conducted using the supercomputer Mogon II and/or advisory services offered by Johannes Gutenberg University Mainz (hpc.uni-mainz.de), which is a member of the AHRP

(Alliance for High Performance Computing in Rhineland Palatinate, www.ahrp.info) and the Gauss Alliance e.V..We also thank 2 anonymous reviewers for improving the quality of the manuscript with their suggestions.

Open Research Section

Datasets for this research are available in these in-text data citation references:

- InSAR: (Fialko & Pearse, 2012),
  https://igppweb.ucsd.edu/~fialko/data.html
- Bouguer anomalies: (Barthelmes & Köhler, 2016),
  http://icgem.gfz-potsdam.de/home
  Model selection: EGM2008,
  Functional selection: gravity_anomaly_bg,
  Grid Step: 0.05°,
  Gaussian Filter: 6 Sigma, 75000 m
- Vs-model: (Ward et al., 2014, 2017),
  https://ds.iris.edu/ds/products/emc-apvcantrfward2014/,
  https://ds.iris.edu/ds/products/emc-apvcpunaantrfward2017/

Software for this research is available on zenodo at:

- LaMEM: (Kaus et al., 2016),
  http://doi.org/10.5281/zenodo.4419782
- geomIO: (Bauville & Baumann, 2019),
  http://doi.org/10.5281/zenodo.4339050

References

Ajtai, N., Ştefănie, H. I., Stoian, L. C., & Oprea, M. G. (2010). The volcanic ash and its impact on European air transport industry. A case study on the detection and impact of the the Eyjafjallajökull volcanic ash plume over North-Western Europe between 14th and 21st April 2010. *Advances in Environmental Sciences*, *2*(1), 57–68.

Barthelmes, F., & Köhler, W. (2016). International centre for global earth models (ICGEM), in: The geodesists handbook 2016. *Journal of Geodesy (2016)*, *90*(10), 907–1205.

Baumann, T., & Kaus, B. J. P. (2015). Geodynamic inversion to constrain the non-linear rheology of the lithosphere. *Geophysical Journal International*, *202*(2), 1289–1316.

Bauville, A., & Baumann, T. S. (2019). geomio: An open-source MATLAB toolbox to create the initial configuration of 2D/3D thermo-mechanical simulations from 2-D vector drawings. *Geochemistry, Geophysics, Geosystems*, *20*(3), 1665–1675. Retrieved from `https://agupubs.onlinelibrary.wiley.com/doi/abs/10.1029/2018GC008057` doi: 10.1029/2018GC008057

Brasse, H., Lezaeta, P., Rath, V., Schwalenberg, K., Soyer, W., & Haak, V. (2002). The Bolivian altiplano conductivity anomaly. *Journal of Geophysical Research: Solid Earth*, *107*(B5). doi: 10.1029/2001JB000391

Breitkreuz, C., & Zeil, W. (1984). Geodynamic and magmatic stages on a traverse through the Andes between 20 and 24 S (N Chile, S Bolivia, NW Argentina). *Journal of the Geological Society*, *141*(5), 861–868.

Byerlee, J. (1978). Friction of rocks. In *Rock friction and earthquake prediction* (pp. 615–626). Birkhäuser, Basel.

Chmielowski, J., Zandt, G., & Haberland, C. (1999). The central Andean Altiplano-Puna magma body. *Geophysical Research Letters*, *26*(6), 783–786.

Comeau, M. J., Unsworth, M. J., & Cordell, D. (2016). New constraints on the magma distribution and composition beneath Volcán Uturuncu and the southern Bolivian Altiplano from magnetotelluric data. *Geosphere*, *12*(5), 1391–1421. doi: 10.1130/GES01277.1

Comeau, M. J., Unsworth, M. J., Ticona, F., & Sunagua, M. (2015). Magnetotelluric images of magma distribution beneath Volcán Uturuncu, Bolivia: Implications for magma dynamics. *Geology*, *43*(3), 243–246. doi: 10.1130/G36258.1

Crameri, F. (2018). Scientific colour-maps. *Zenodo..DOI: https://doi.org/10.5281/zenodo*, *1243862*.

Crameri, F., Schmeling, H., Golabek, G. J., Duretz, T., Orendt, R., Buiter, S., ... Tackley, P. (2012). A comparison of numerical surface topography calculations in geodynamic modelling: an evaluation of the 'sticky air'method. *Geophysical Journal International*, *189*(1), 38–54.

De Silva, S. (1989). Altiplano-Puna volcanic complex of the central Andes. *Geology*, *17*(12), 1102–1106.

Drucker, D. C., & Prager, W. (1952). Soil mechanics and plastic analysis or limit design. *Quarterly of applied mathematics*, *10*(2), 157–165.

Duretz, T., May, D. A., Gerya, T., & Tackley, P. (2011). Discretization errors and free surface stabilization in the finite difference and marker-in-cell method for applied geodynamics: A numerical study. *Geochemistry, Geophysics, Geosystems*, *12*(7). doi: 10.1029/2011GC003567

Fialko, Y., & Pearse, J. (2012). Sombrero uplift above the Altiplano-Puna magma body: Evidence of a ballooning mid-crustal diapir. *Science*, *338*(6104), 250–

252. doi: 10.1126/science.1226358

Fialko, Y., Simons, M., & Agnew, D. (2001). The complete (3-D) surface displacement field in the epicentral area of the 1999 mw7.1 Hector Mine earthquake, California, from space geodetic observations. *Geophysical research letters*, *28*(16), 3063–3066.

Gercek, H. (2007). Poisson's ratio values for rocks. *International Journal of Rock Mechanics and Mining Sciences*, *44*(1), 1–13. doi: 10.1016/j.ijrmms.2006.04.011

Godoy, B., Wörner, G., Kojima, S., Aguilera, F., Simon, K., & Hartmann, G. (2014). Low-pressure evolution of arc magmas in thickened crust: The San Pedro–Linzor volcanic chain, Central Andes, northern Chile. *Journal of south american earth sciences*, *52*, 24–42.

Godoy, B., Wörner, G., Le Roux, P., de Silva, S., Parada, M. Á., Kojima, S., ... Martínez, P. (2017). Sr-and Nd-isotope variations along the Pleistocene San Pedro–Linzor volcanic chain, N. Chile: Tracking the influence of the upper crustal Altiplano-Puna Magma Body. *Journal of Volcanology and Geothermal Research*, *341*, 172–186. doi: 10.1016/j.jvolgeores.2017.05.030

Gottsmann, J., Blundy, J., Henderson, S. T., Pritchard, M. E., & Sparks, R. (2017). Thermomechanical modeling of the Altiplano-Puna deformation anomaly: Multiparameter insights into magma mush reorganization. *Geosphere*, *13*(4), 1042–1065. doi: 10.1130/GES01420.1

Gottsmann, J., del Potro, R., & Muller, C. (2018). 50 years of steady ground deformation in the altiplano-puna region of southern Bolivia. *Geosphere*, *14*(1), 65–73. doi: 10.1130/GES01570.1

Götze, H.-J., & Kirchner, A. (1997). Interpretation of gravity and geoid in the Central Andes between 20 and 29 s. *Journal of South American Earth Sciences*, *10*(2), 179–188.

Götze, H.-J., & Krause, S. (2002). The Central Andean gravity high, a relic of an old subduction complex? *Journal of South American Earth Sciences*, *14*(8), 799–811.

Harlow, F. H., & Welch, J. E. (1965). Numerical calculation of time-dependent viscous incompressible flow of fluid with free surface. *The physics of fluids*, *8*(12), 2182–2189.

Hedenquist, J. W., & Lowenstern, J. B. (1994). The role of magmas in the formation of hydrothermal ore deposits. *Nature*, *370*(6490), 519–527.

Heit, B., Koulakov, I., Asch, G., Yuan, X., Kind, R., Alcocer-Rodriguez, I., ... Wilke, H. (2008). More constraints to determine the seismic structure beneath the Central Andes at 21 s using teleseismic tomography analysis. *Journal of South American Earth Sciences*, *25*(1), 22–36.

Henderson, S. T., & Pritchard, M. E. (2013). Decadal volcanic deformation in the Central Andes Volcanic Zone revealed by InSAR time series. *Geochemistry, Geophysics, Geosystems*, *14*(5), 1358–1374. doi: 10.1002/ggge.20074

Henderson, S. T., & Pritchard, M. E. (2017). Time-dependent deformation of Uturuncu volcano, Bolivia, constrained by GPS and InSAR measurements and implications for source models. *Geosphere*, *13*(6), 1834–1854. doi: 10.1130/GES01203.1

Hickey, J., & Gottsmann, J. (2014). Benchmarking and developing numerical Finite Element models of volcanic deformation. *Journal of Volcanology and Geothermal Research*, *280*, 126–130.

Hickey, J., Gottsmann, J., & del Potro, R. (2013). The large-scale surface uplift in the Altiplano-Puna region of Bolivia: A parametric study of source characteristics and crustal rheology using finite element analysis. *Geochemistry, Geophysics, Geosystems*, *14*(3), 540–555.

Hickey, J., Gottsmann, J., Nakamichi, H., & Iguchi, M. (2016). Thermomechanical controls on magma supply and volcanic deformation: application to Aira caldera, japan. *Scientific reports*, *6*(1), 1–10.

Hoek, E., & Brown, E. T. (1997). Practical estimates of rock mass strength. *International journal of rock mechanics and mining sciences*, *34*(8), 1165–1186.

Ibarra, F., Liu, S., Meeßen, C., Prezzi, C., Bott, J., Scheck-Wenderoth, M., ... Strecker, M. (2019). 3D data-derived lithospheric structure of the Central Andes and its implications for deformation: Insights from gravity and geodynamic modelling. *Tectonophysics*, *766*, 453–468.

Jang, H.-S., Zhang, Q.-Z., Kang, S.-S., & Jang, B.-A. (2018). Determination of the basic friction angle of rock surfaces by tilt tests. *Rock Mechanics and Rock Engineering*, *51*(4), 989–1004.

Jay, J. A., Pritchard, M. E., West, M. E., Christensen, D., Haney, M., Minaya, E.,

... Zabala, M. (2012). Shallow seismicity, triggered seismicity, and ambient noise tomography at the long-dormant Uturuncu Volcano, Bolivia. *Bulletin of Volcanology*, *74*(4), 817–837.

Kaus, B. J. P., Mühlhaus, H., & May, D. A. (2010). A stabilization algorithm for geodynamic numerical simulations with a free surface. *Physics of the Earth and Planetary Interiors*, *181*(1-2), 12–20.

Kaus, B. J. P., Popov, A. A., Baumann, T., Pusok, A., Bauville, A., Fernandez, N., & Collignon, M. (2016). Forward and inverse modelling of lithospheric deformation on geological timescales. In *Proceedings of nic symposium.*

Kay, S. M., Coira, B. L., Caffe, P. J., & Chen, C.-H. (2010). Regional chemical diversity, crustal and mantle sources and evolution of central Andean Puna plateau ignimbrites. *Journal of Volcanology and Geothermal Research*, *198*(1-2), 81–111.

Kiyoo, M. (1958). Relations between the eruptions of various volcanoes and the deformations of the ground surfaces around them. *Earthq Res Inst*, *36*, 99–134.

Kühn, C., Brasse, H., & Schwarz, G. (2018). Three-dimensional electrical resistivity image of the volcanic arc in Northern Chile—an appraisal of early magnetotelluric data. *Pure and Applied Geophysics*, *175*(6), 2153–2165.

Kukarina, E., West, M., Hutchinson Keyson, L., Koulakov, I., Tsibizov, L., & Smirnov, S. (2017). Focused magmatism beneath Uturuncu volcano, Bolivia: Insights from seismic tomography and deformation modeling. *Geosphere*, *13*(6), 1855–1866. doi: 10.1130/GES01403.1

Laske, G., Masters, G., Ma, Z., & Pasyanos, M. (2013). Update on CRUST1. 0–A 1-degree global model of Earth's crust. In *Geophys. Res. Abstr* (Vol. 15, p. 2658).

Lau, N., Tymofyeyeva, E., & Fialko, Y. (2018). Variations in the long-term uplift rate due to the Altiplano–Puna magma body observed with Sentinel-1 interferometry. *Earth and Planetary Science Letters*, *491*, 43–47.

Laumonier, M., Gaillard, F., Muir, D., Blundy, J., & Unsworth, M. (2017). Giant magmatic water reservoirs at mid-crustal depth inferred from electrical conductivity and the growth of the continental crust. *Earth and Planetary Science Letters*, *457*, 173–180.

McFarlin, H., Christensen, D., McNutt, S. R., Ward, K. M., Ryan, J., Zandt, G., &

Thompson, G. (2018). Receiver function analyses of Uturuncu volcano, Bolivia and vicinity. *Geosphere*, *14*(1), 50–64.

Michelfelder, G. S., Feeley, T. C., & Wilder, A. D. (2014). The volcanic evolution of Cerro Uturuncu: A high-K, composite volcano in the back-arc of the central Andes of SW Bolivia. *International Journal of Geosciences*, *5*(11), 1263–1281.

Muir, D. D., Blundy, J. D., Hutchinson, M. C., & Rust, A. C. (2014a). Petrological imaging of an active pluton beneath Cerro Uturuncu, Bolivia. *Contributions to Mineralogy and Petrology*, *167*(3), 980.

Muir, D. D., Blundy, J. D., Rust, A. C., & Hickey, J. (2014b). Experimental constraints on dacite pre-eruptive magma storage conditions beneath Uturuncu volcano. *Journal of Petrology*, *55*(4), 749–767.

Naranjo, J., Sigurdsson, H., Carey, S., & Fritz, W. (1986). Eruption of the Nevado del Ruiz volcano, Colombia, on 13 November 1985: tephra fall and lahars. *Science*, *233*(4767), 961–963.

Oncken, O., Asch, G., Haberland, C., Metchie, J., Sobolev, S., Stiller, M., ... Rietbrock, A. (2003). Seismic imaging of a convergent continental margin and plateau in the central Andes (Andean Continental Research Project 1996 (ANCORP'96)). *Journal of Geophysical Research: Solid Earth*, *108*(B7).

Pearse, J., & Fialko, Y. (2010). Mechanics of active magmatic intraplating in the Rio Grande Rift near Socorro, New Mexico. *Journal of Geophysical Research: Solid Earth*, *115*(B7).

Perkins, J. P., Ward, K. M., De Silva, S. L., Zandt, G., Beck, S. L., & Finnegan, N. J. (2016). Surface uplift in the Central Andes driven by growth of the Altiplano Puna Magma Body. *Nature Communications*, *7*(1), 1–10.

Potro, R., Díez, M., Blundy, J., Camacho, A. G., & Gottsmann, J. (2013). Diapiric ascent of silicic magma beneath the Bolivian Altiplano. *Geophysical Research Letters*, *40*(10), 2044–2048.

Prezzi, C. B., Götze, H.-J., & Schmidt, S. (2009). 3D density model of the Central Andes. *Physics of the Earth and Planetary Interiors*, *177*(3-4), 217–234.

Pritchard, M. E., de Silva, S., Michelfelder, G., Zandt, G., McNutt, S., Gottsmann, J., ... Ward, K. M. (2018). Synthesis: Plutons: Investigating the relationship between pluton growth and volcanism in the Central Andes. *Geosphere*, *14*(3), 954–982.

Pritchard, M. E., & Gregg, P. M. (2016). Geophysical evidence for silicic crustal melt in the continents: where, what kind, and how much? *Elements*, *12*(2), 121–127.

Pritchard, M. E., & Simons, M. (2002). A satellite geodetic survey of large-scale deformation of volcanic centres in the central Andes. *Nature*, *418*(6894), 167–171.

Pritchard, M. E., & Simons, M. (2004). An InSAR-based survey of volcanic deformation in the central Andes. *Geochemistry, Geophysics, Geosystems*, *5*(2). doi: 10.1029/2003GC000610

Reuber, G. S., Kaus, B. J. P., Popov, A. A., & Baumann, T. S. (2018b). Unraveling the physics of the yellowstone magmatic system using geodynamic simulations. *Frontiers in Earth Science*, *6*, 117. doi: 10.3389/feart.2018.00117

Reuber, G. S., Popov, A. A., & Kaus, B. J. P. (2018a). Deriving scaling laws in geodynamics using adjoint gradients. *Tectonophysics*, *746*, 352–363.

Sambridge, M. (1999a). Geophysical inversion with a neighbourhood algorithm–I. Searching a parameter space. *Geophysical Journal International*, *138*(2), 479–494.

Sambridge, M. (1999b). Geophysical inversion with a neighbourhood algorithm–II. Appraising the ensemble. *Geophysical Journal International*, *138*(3), 727–746.

Schilling, F. R., Trumbull, R. B., Brasse, H., Haberland, C., Asch, G., Bruhn, D., ... Vietor, T. (2006). Partial melting in the Central Andean crust: a review of geophysical, petrophysical, and petrologic evidence. In *The andes* (pp. 459–474). Springer.

Schwarz, G., Haak, V., Martinez, E., & Bannister, J. (1984). The electrical conductivity of the Andean crust in northern Chile and southern Bolivia as inferred from magnetotelluric measurements. *Journal of Geophysics*, *55*(1), 169–178.

Schwarz, G., & Krüger, D. (1997). Resistivity cross section through the southern central Andes as inferred from magnetotelluric and geomagnetic deep soundings. *Journal of Geophysical Research: Solid Earth*, *102*(B6), 11957–11978.

Sparks, R. S. J., Folkes, C. B., Humphreys, M. C., Barfod, D. N., Clavero, J., Sunagua, M. C., ... Pritchard, M. E. (2008). Uturuncu volcano, Bolivia: Volcanic unrest due to mid-crustal magma intrusion. *American Journal of Science*, *308*(6), 727–769.

Talwani, M., Worzel, J. L., & Landisman, M. (1959). Rapid gravity computations for two-dimensional bodies with application to the Mendocino submarine fracture zone. *Journal of geophysical research*, *64*(1), 49–59.

Tassara, A., & Echaurren, A. (2012). Anatomy of the Andean subduction zone: three-dimensional density model upgraded and compared against global-scale models. *Geophysical Journal International*, *189*(1), 161–168.

Tassara, A., Götze, H.-J., Schmidt, S., & Hackney, R. (2006). Three-dimensional density model of the Nazca plate and the Andean continental margin. *Journal of Geophysical Research: Solid Earth*, *111*(B9). doi: 10.1029/2005JB003976

Walter, T. R., & Motagh, M. (2014). Deflation and inflation of a large magma body beneath Uturuncu volcano, Bolivia? Insights from InSAR data, surface lineaments and stress modelling. *Geophysical Journal International*, *198*(1), 462–473.

Ward, K. M., Delph, J. R., Zandt, G., Beck, S. L., & Ducea, M. N. (2017). Magmatic evolution of a Cordilleran flare-up and its role in the creation of silicic crust. *Scientific reports*, *7*(1), 1–8. doi: 10.1038/s41598-017-09015-5

Ward, K. M., Zandt, G., Beck, S. L., Christensen, D. H., & McFarlin, H. (2014). Seismic imaging of the magmatic underpinnings beneath the Altiplano-Puna volcanic complex from the joint inversion of surface wave dispersion and receiver functions. *Earth and Planetary Science Letters*, *404*, 43–53.

Wessel, P., Smith, W. H., Scharroo, R., Luis, J., & Wobbe, F. (2013). Generic mapping tools: improved version released. *Eos, Transactions American Geophysical Union*, *94*(45), 409–410.

Wigger, P. J. (1988). Seismicity and crustal structure of the Central Andes. In *The southern central Andes* (pp. 209–229). Springer, Berlin, Heidelberg.

Wörner, G., Mamani, M., & Blum-Oeste, M. (2018). Magmatism in the Central Andes. *Elements: An International Magazine of Mineralogy, Geochemistry, and Petrology*, *14*(4), 237–244.

Yuan, X., Sobolev, S. V., Kind, R., Oncken, O., Bock, G., Asch, G., ... Comte, D. (2000). Subduction and collision processes in the Central Andes constrained by converted seismic phases. *Nature*, *408*(6815), 958–961.

Zandt, G., Leidig, M., Chmielowski, J., Baumont, D., & Yuan, X. (2003). Seismic detection and characterization of the Altiplano-Puna magma body, central

Andes. *Pure and Applied Geophysics*, *160*(3-4), 789–807.

Supporting Information References

References

Kress, V. C., & Carmichael, I. S. (1991). The compressibility of silicate liquids containing Fe 2 O 3 and the effect of composition, temperature, oxygen fugacity and pressure on their redox states. *Contributions to Mineralogy and Petrology*, *108*(1-2), 82–92.

Lange, R. A., & Carmichael, I. S. (1987). Densities of Na2O-K2O-CaO-MgO-FeO-Fe2O3-Al2O3-TiO2-SiO2 liquids: new measurements and derived partial molar properties. *Geochimica et Cosmochimica Acta*, *51*(11), 2931–2946.

Mackwell, S., Zimmerman, M., & Kohlstedt, D. (1998). High-temperature deformation of dry diabase with application to tectonics on Venus. *Journal of Geophysical Research: Solid Earth*, *103*(B1), 975–984.

Ochs, F. A., & Lange, R. A. (1999). The density of hydrous magmatic liquids. *Science*, *283*(5406), 1314–1317.

Ranalli, G. (1995). *Rheology of the Earth*. Springer Science & Business Media.

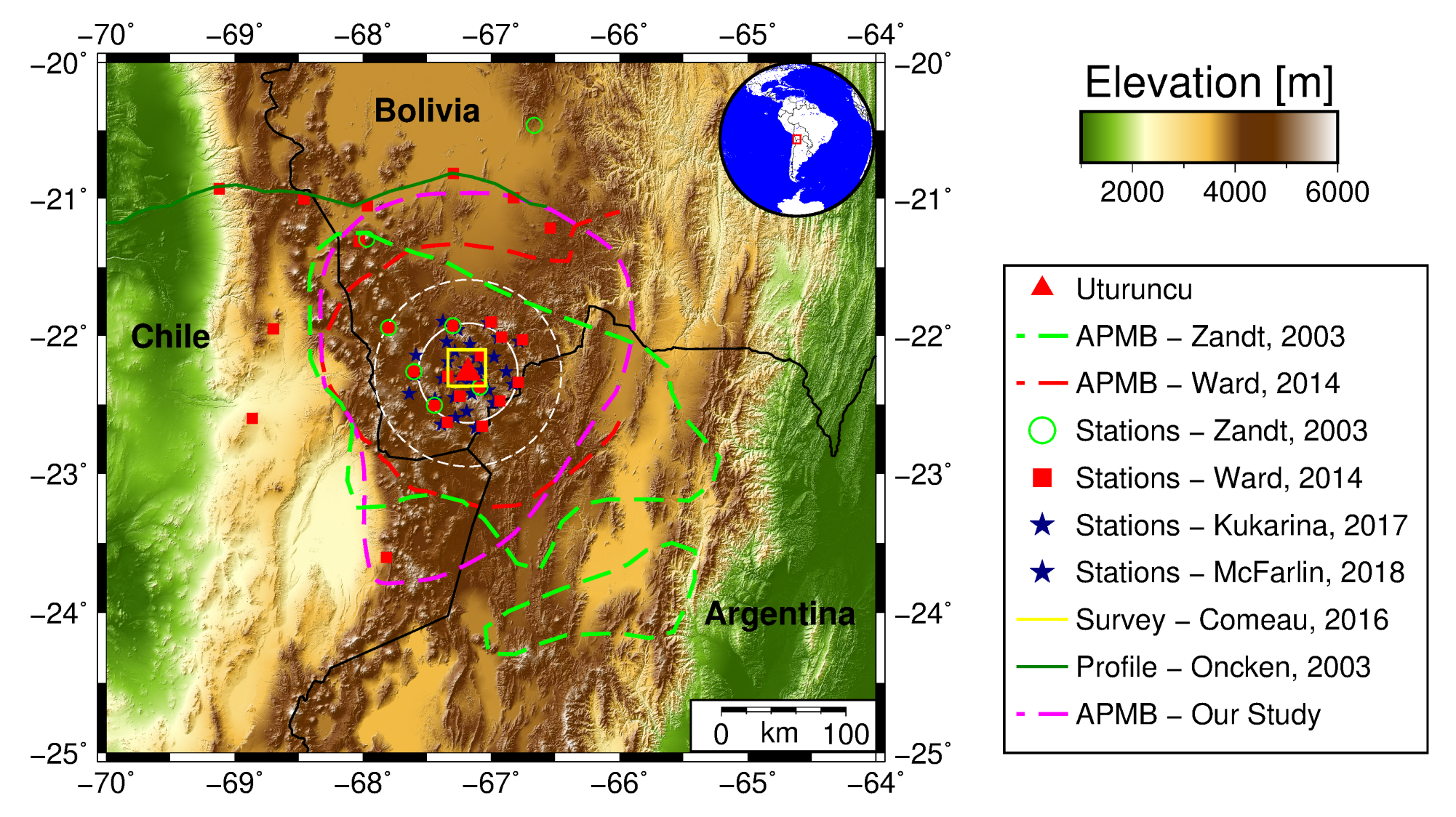
−70°
−69°
−68°
−67°
−66°
−65°
−64°
−20°
−21°
−22°
−23°
−24°
−25°
Bolivia
Chile
Argentina
0 km 100
Elevation [m]
2000
4000
6000
Uturuncu
APMB – Zandt, 2003
APMB – Ward, 2014
Stations – Zandt, 2003
Stations – Ward, 2014
Stations – Kukarina, 2017
Stations – McFarlin, 2018
Survey – Comeau, 2016
Profile – Oncken, 2003
APMB – Our Study

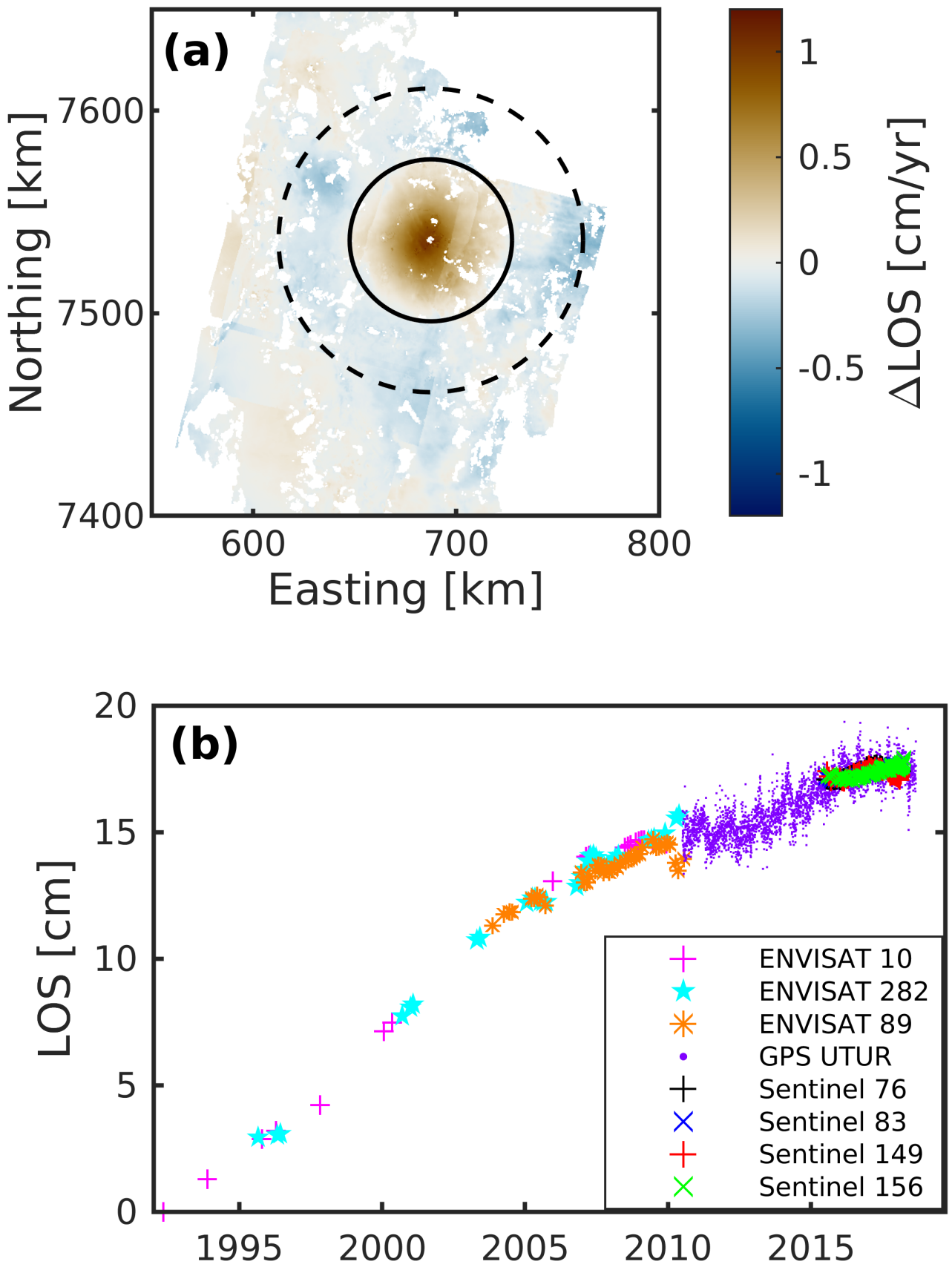
(a)
7600
7500
7400
Northing [km]
600
700
800
Easting [km]
1
0.5
0
-0.5
-1
ΔLOS [cm/yr]
(b)
20
15
10
5
0
LOS [cm]
1995
2000
2005
2010
2015
ENVISAT 10
ENVISAT 282
ENVISAT 89
GPS UTUR
Sentinel 76
Sentinel 83
Sentinel 149
Sentinel 156

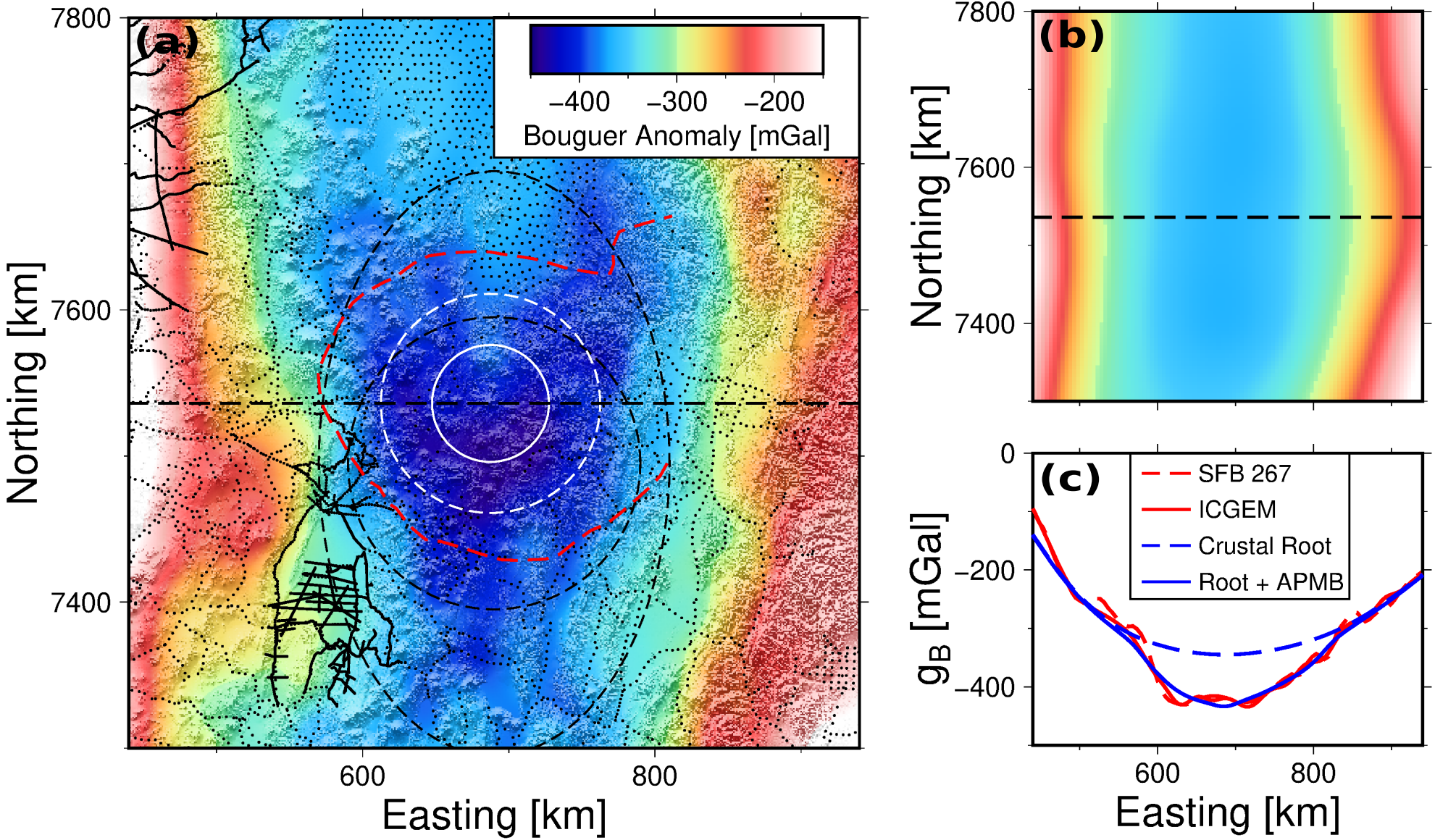
(a)
−400
−300
−200
Bouguer Anomaly [mGal]
7800
7600
7400
Northing [km]
600
800
Easting [km]
(b)
7800
7600
7400
Northing [km]
(c)
SFB 267
ICGEM
Crustal Root
Root + APMB
0
−200
−400
g_B [mGal]
600
800
Easting [km]

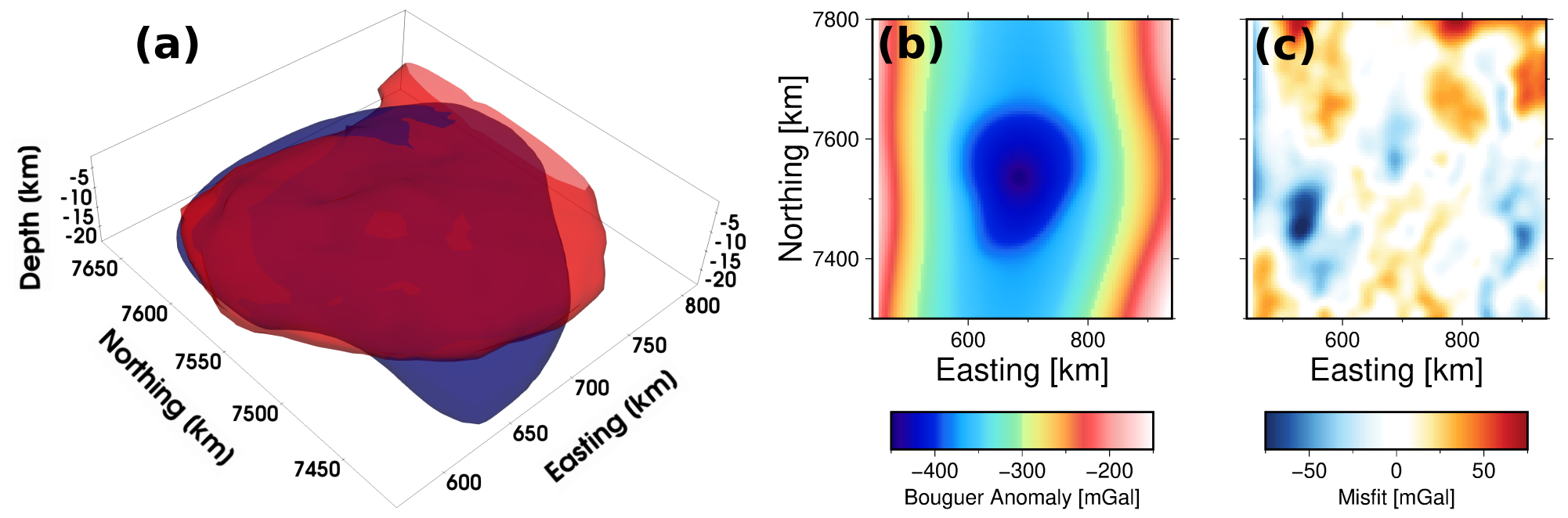
(a)
Depth (km)
-5
-10
-15
-20
7650
7600
7550
7500
7450
Northing (km)
600
650
700
750
800
Easting (km)
(b)
Northing [km]
7800
7600
7400
600
800
Easting [km]
−400
−300
−200
Bouguer Anomaly [mGal]
(c)
600
800
Easting [km]
−50
0
50
Misfit [mGal]

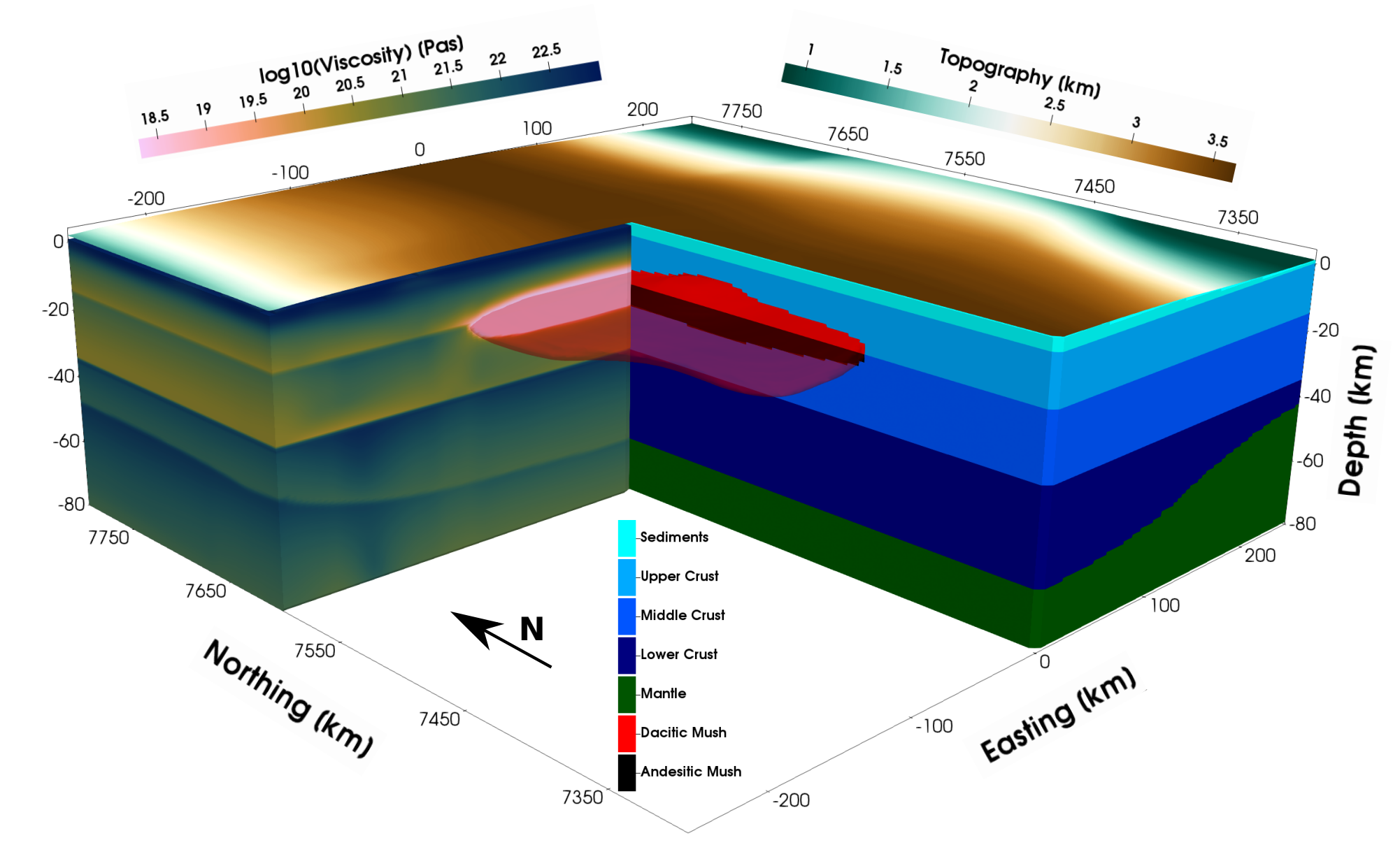
log10(Viscosity) (Pas)
18.5
19
19.5
20
20.5
21
21.5
22
22.5
Topography (km)
1
1.5
2
2.5
3
3.5
Northing (km)
7750
7650
7550
7450
7350
Easting (km)
200
100
0
-100
-200
Depth (km)
0
-20
-40
-60
-80
N
Sediments
Upper Crust
Middle Crust
Lower Crust
Mantle
Dacitic Mush
Andesitic Mush

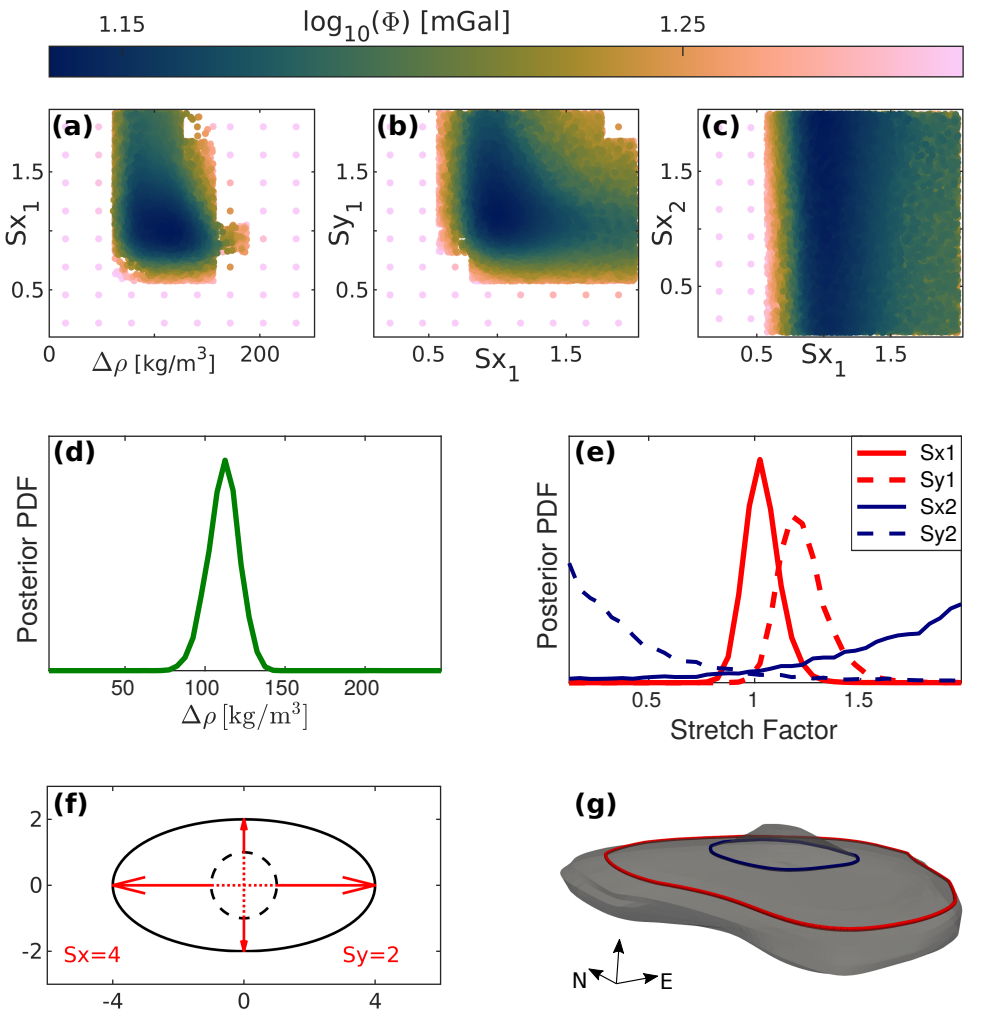
1.15
log10(Φ) [mGal]
1.25
(a)
(b)
(c)
Sx1
Sy1
Sx2
Δρ [kg/m3]
Sx1
Sx1
(d)
Posterior PDF
Δρ [kg/m3]
(e)
Posterior PDF
Sx1
Sy1
Sx2
Sy2
Stretch Factor
(f)
Sx=4
Sy=2
(g)
N
E

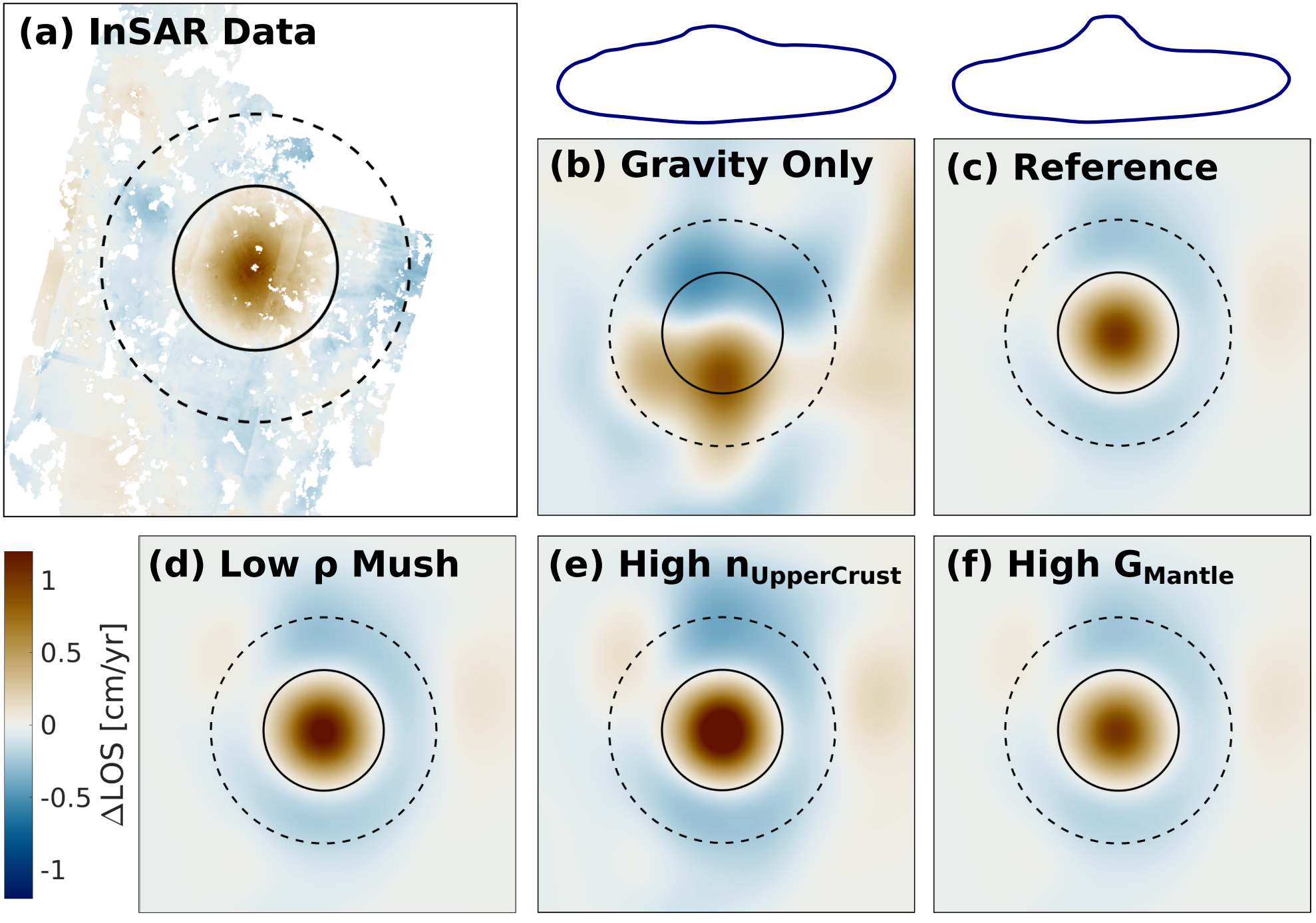
(a) InSAR Data
(b) Gravity Only
(c) Reference
(d) Low ρ Mush
(e) High $n_{UpperCrust}$
(f) High G_{Mantle}
1
0.5
0
-0.5
-1
ΔLOS [cm/yr]

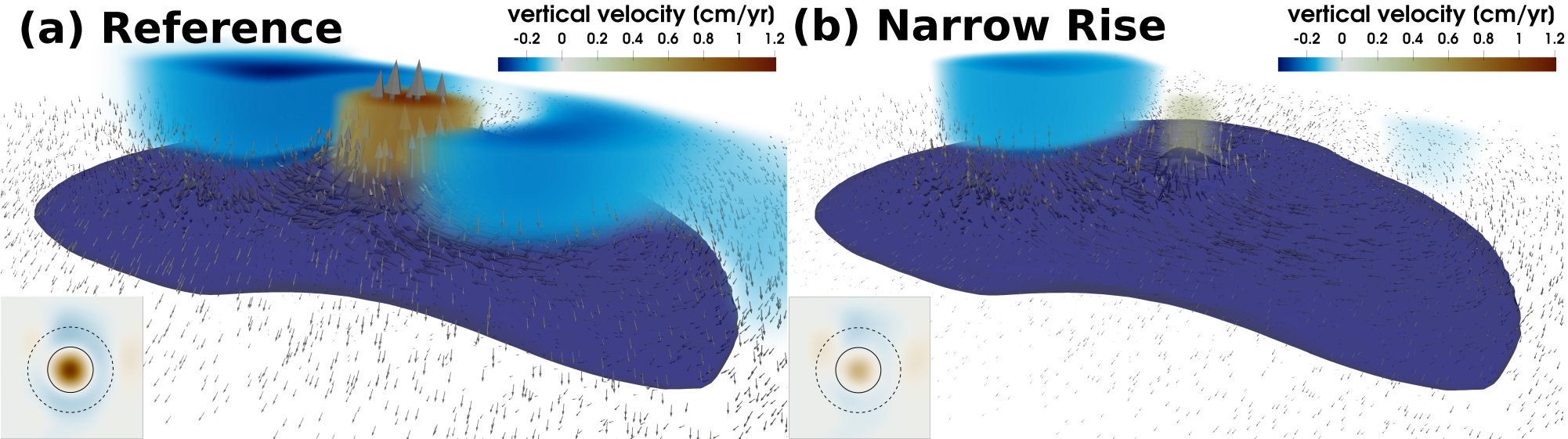
(a) Reference
vertical velocity (cm/yr)
-0.2 0 0.2 0.4 0.6 0.8 1 1.2
(b) Narrow Rise
vertical velocity (cm/yr)
-0.2 0 0.2 0.4 0.6 0.8 1 1.2

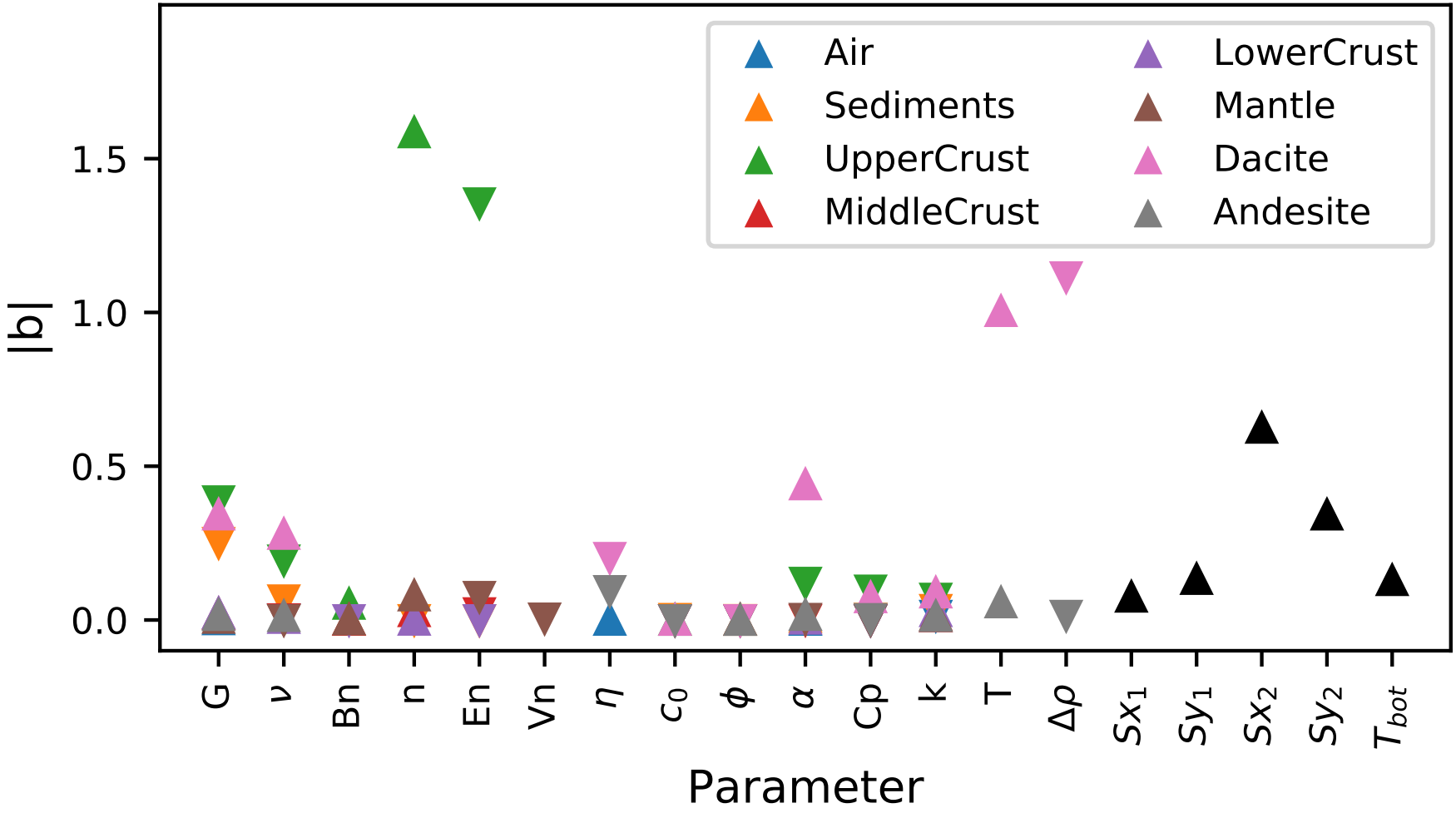
Air
Sediments
UpperCrust
MiddleCrust
LowerCrust
Mantle
Dacite
Andesite
|b|
0.0
0.5
1.0
1.5
G
ν
Bn
n
En
Vn
η
c_0
ϕ
α
Cp
k
T
Δρ
Sx_1
Sy_1
Sx_2
Sy_2
T_{bot}
Parameter

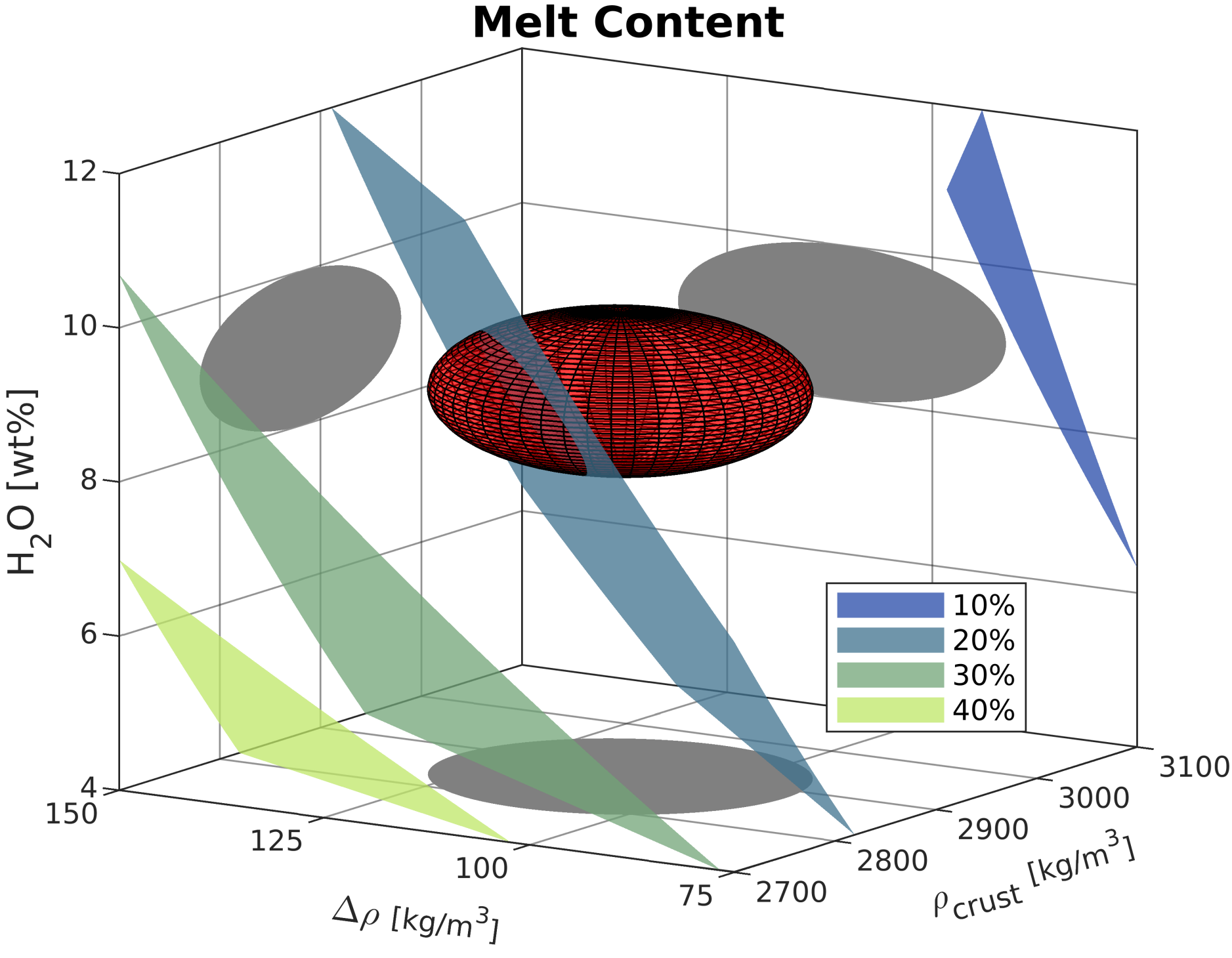
Melt Content
12
10
8
6
4
H_2O [wt%]
150
125
100
75
$\Delta\rho$ [kg/m^3]
2700
2800
2900
3000
3100
ρ_{crust} [kg/m^3]
10%
20%
30%
40%

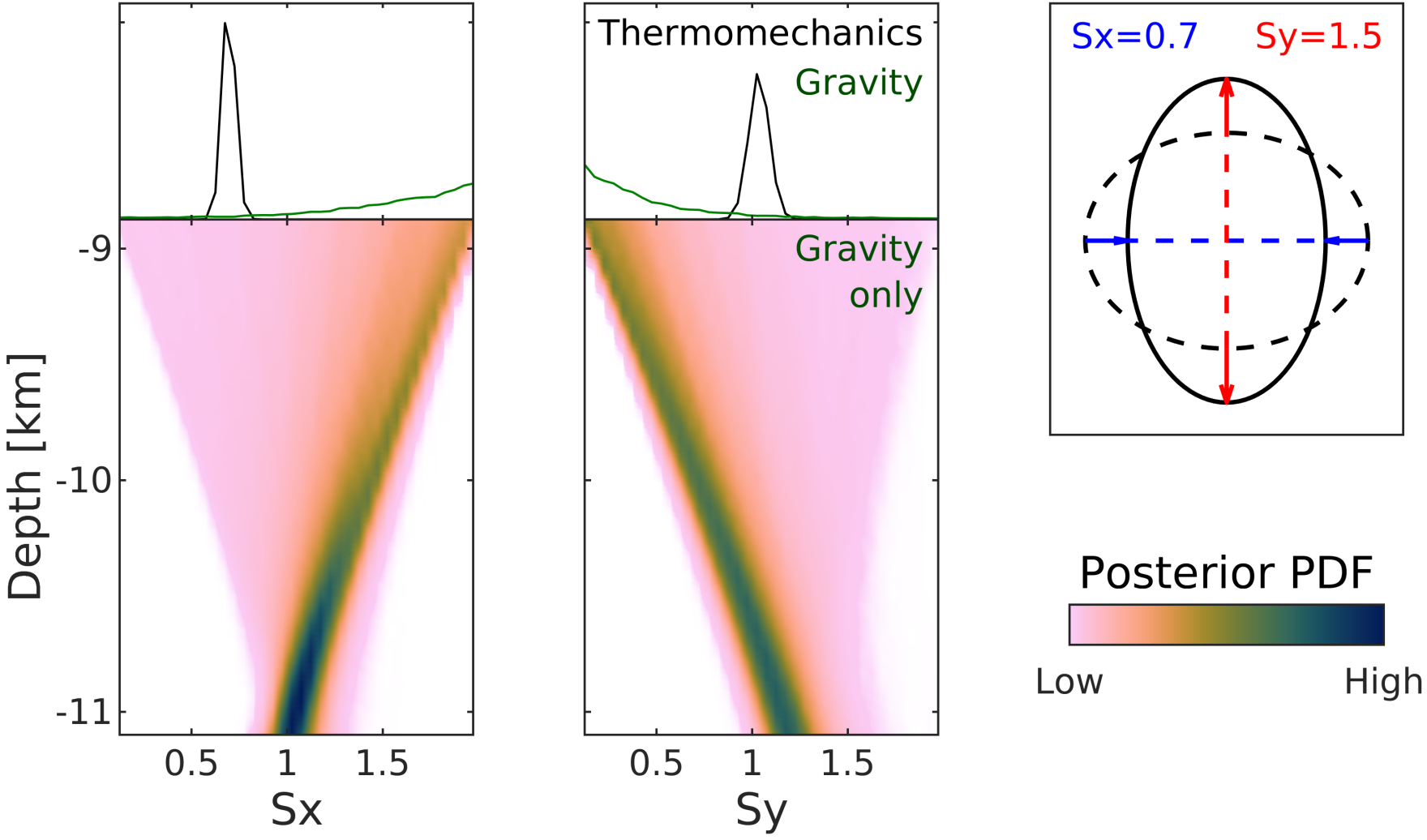
Depth [km]
-9
-10
-11
0.5
1
1.5
Sx
Thermomechanics
Gravity
Gravity
only
0.5
1
1.5
Sy
Sx=0.7
Sy=1.5
Posterior PDF
Low
High

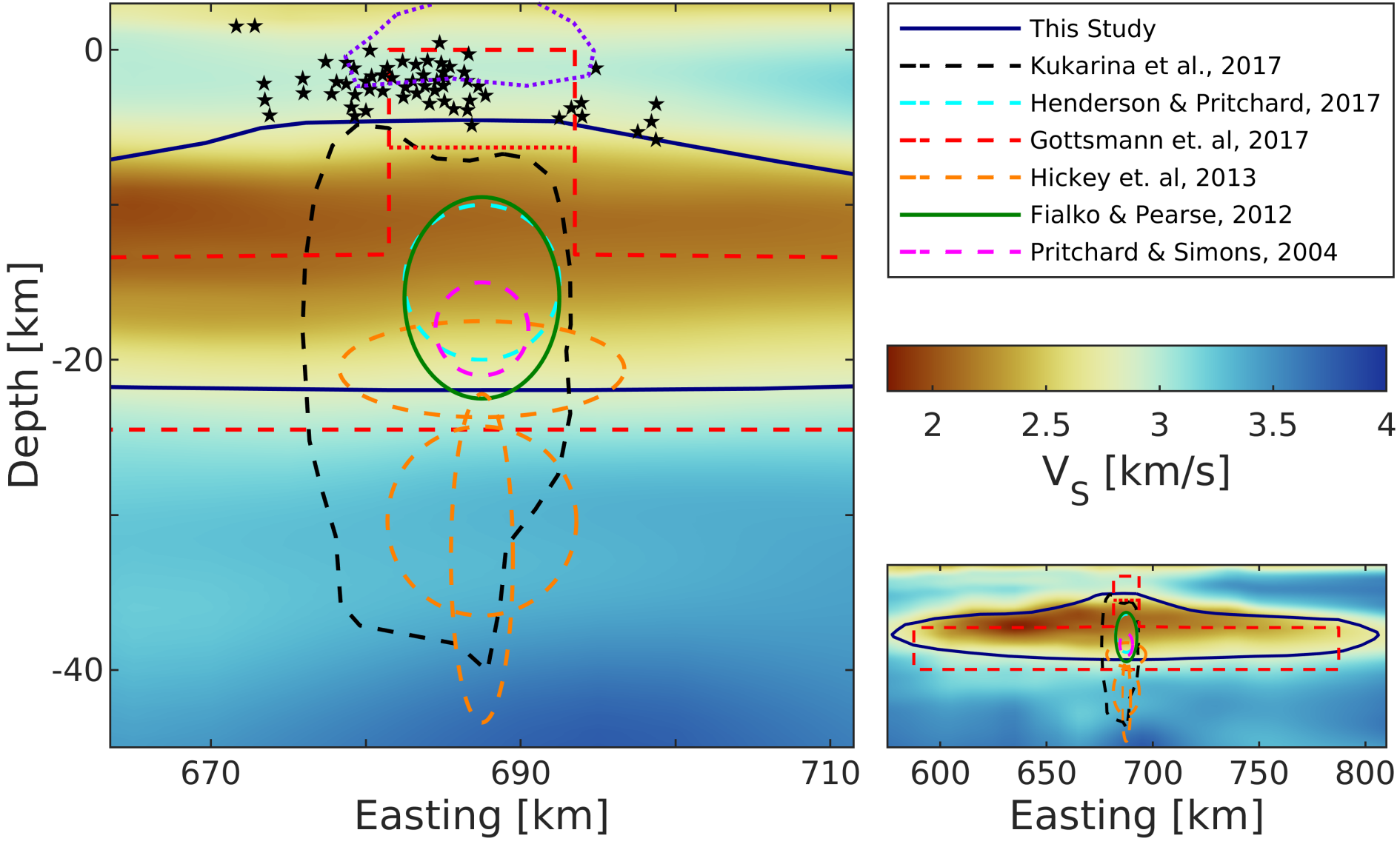
This Study
Kukarina et al., 2017
Henderson & Pritchard, 2017
Gottsmann et. al, 2017
Hickey et. al, 2013
Fialko & Pearse, 2012
Pritchard & Simons, 2004
0
-20
-40
Depth [km]
670
690
710
Easting [km]
2
2.5
3
3.5
4
V_S [km/s]
600
650
700
750
800
Easting [km]